Imaging Black Holes

Past, Present, and Future with the Event Horizon Telescope

Violette Impellizeri

on behalf of the EHT collaboration

Event Horizon Telescope

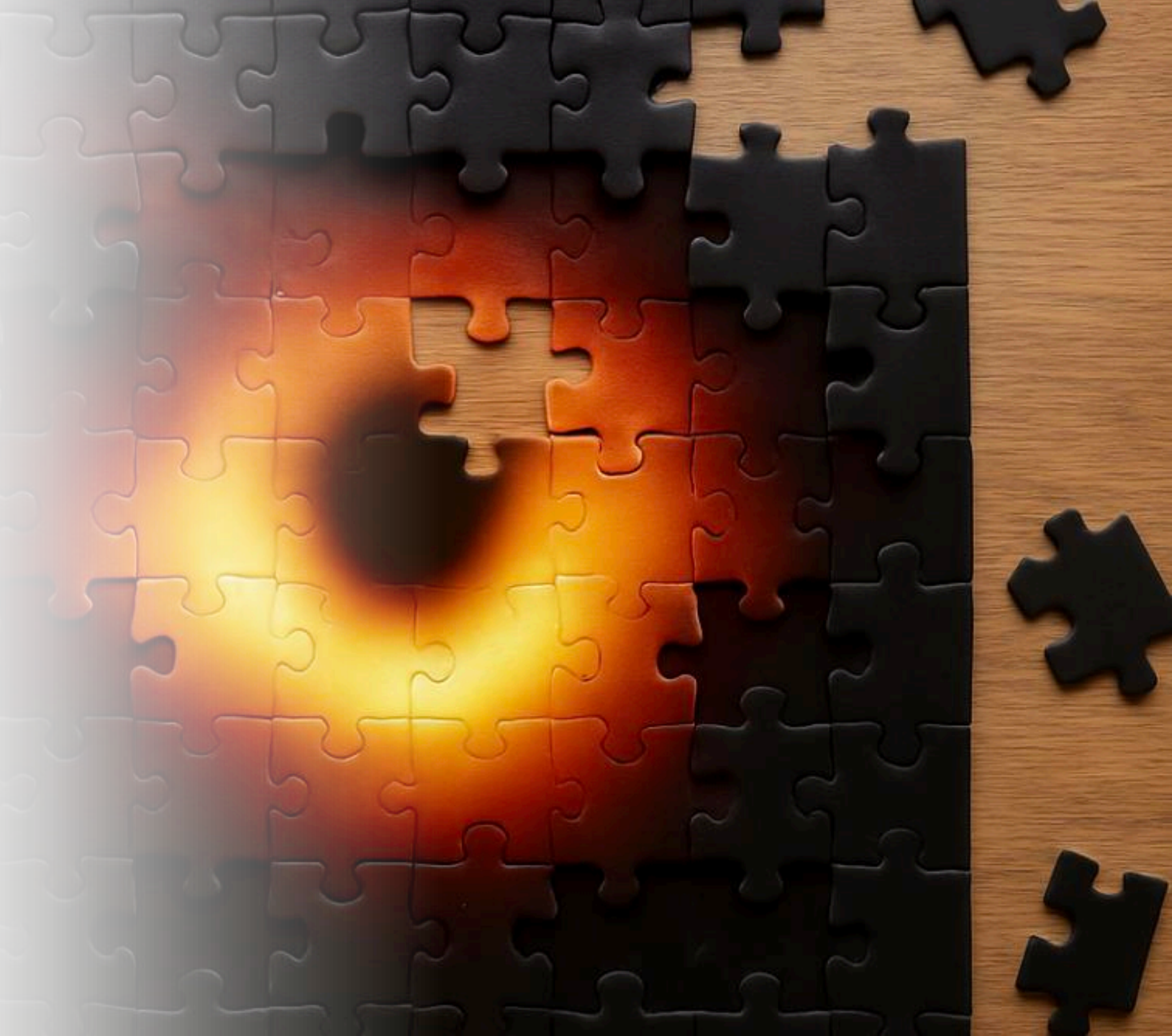

EHT COLLABORATION MEETING 2024

GROUP PICTURE

Unidad de Posgrado, UNAM, Mexico City, Mex

The radio sky is dominated by bright radio galaxies in far universe

Radio sky over Green Bank radio telescopes

Moon to scale on LOFAR field

Hercules A = 3C348
at 1 billion light years,
observed with the VLA

Mess

Hubble

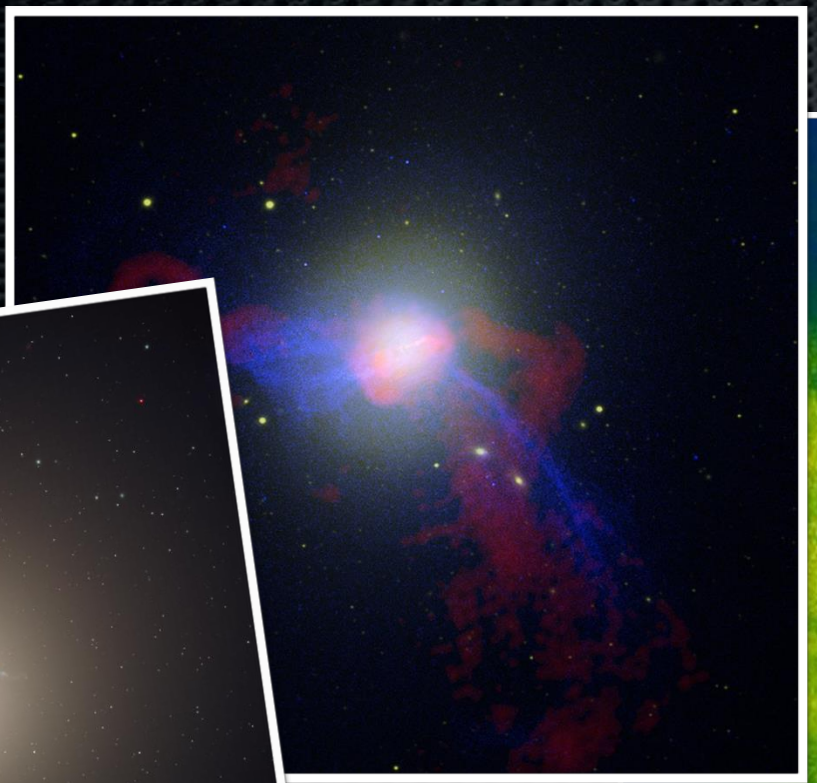

LOFAR + optical

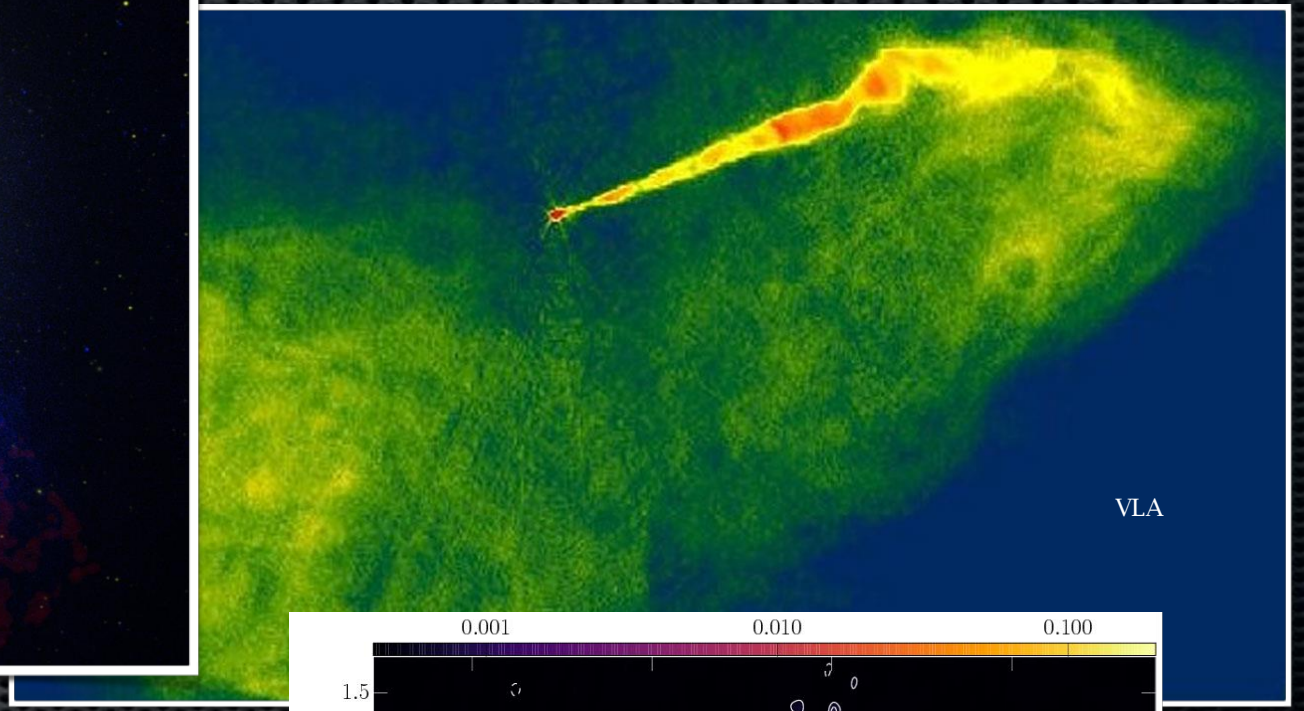

VLA

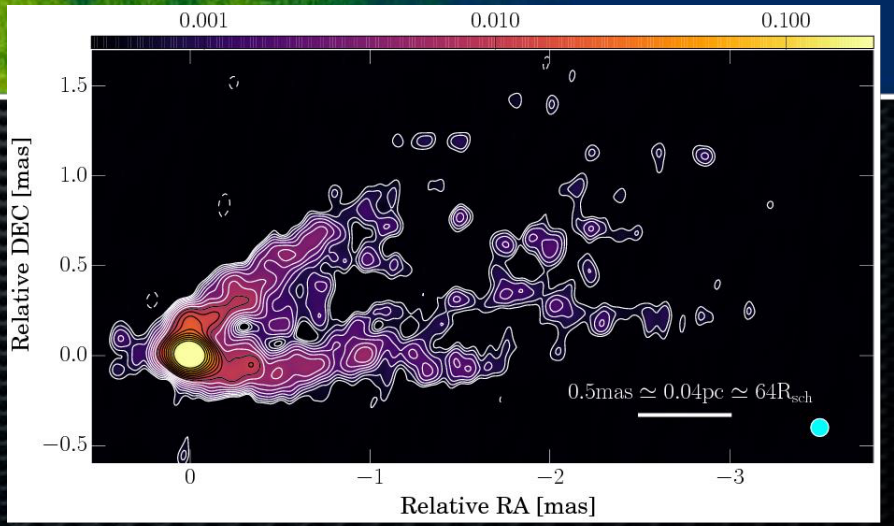

VLBI

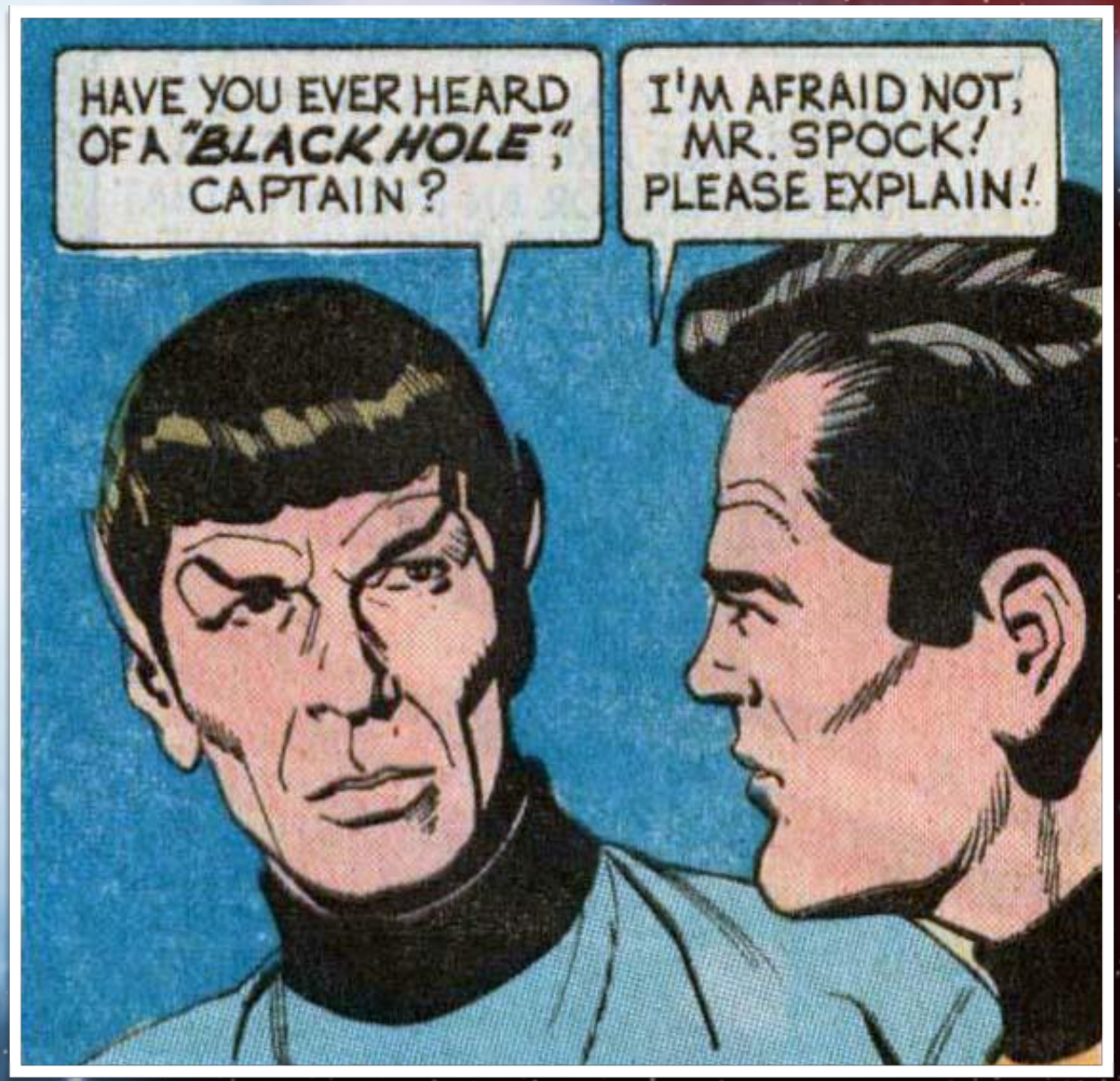
HAVE YOU EVER HEARD OF A "BLACK HOLE", CAPTAIN?
I'M AFRAID NOT, MR. SPOCK! PLEASE EXPLAIN!

Resolving the Black Hole shadow

$\rightarrow \theta_{shadow} \sim 10\ GM/Dc^2 \sim 20 - 40\ \mu as\ (M87)$
$\sim 50\ \mu as\ (Sgr\ A^*)$

- Typical VLBI network 3000km baselines at 22 GHz: $\theta \leq 1$ mas
- Largest apparent Black Holes:
  - Schwarzschild radius SgrA* $4.5\ 10^6\ M_\odot$ at 8 kpc: 10μas
  - Or for M87 $3.5\ 10^9\ M_\odot$ at 16.4 Mpc: 4.2μas
  - Or for M87 $6.5\ 10^9\ M_\odot$ at 16.4 Mpc: 7.8μas

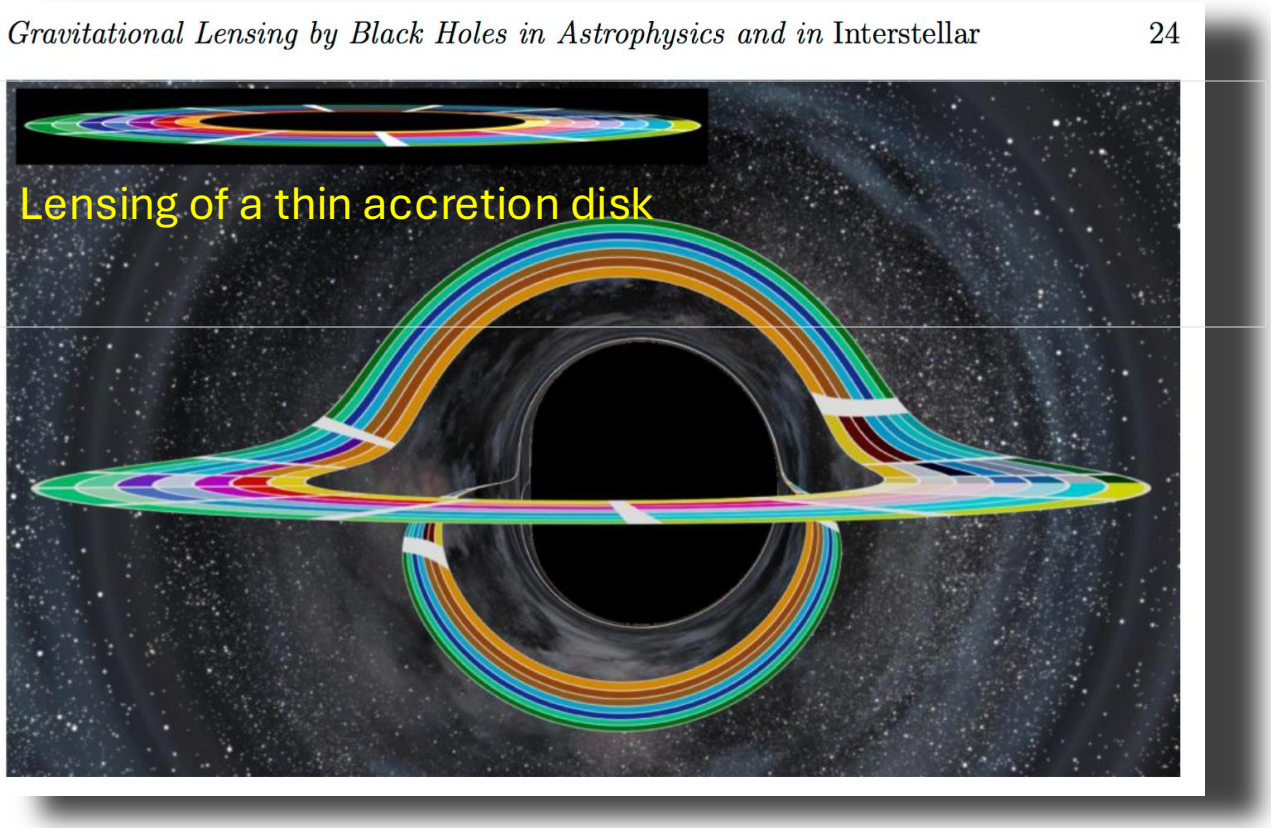

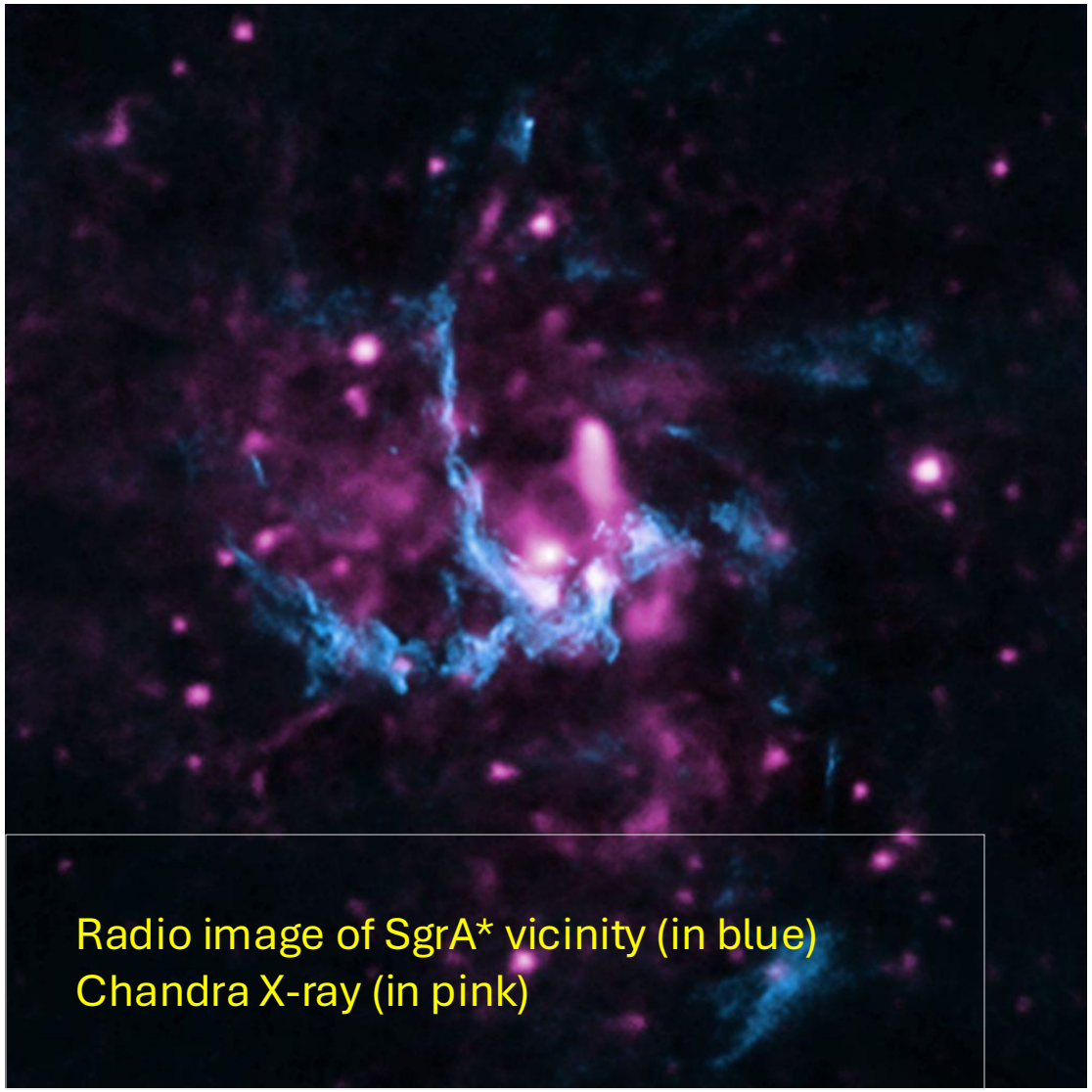

Practical Challenges of BH Imaging

- Need ultra-high resolution → Short wavelength, long baselines
- Atmosphere is a limitation → Only the highest, driest places will do
- Sensitivity starved → The biggest telescopes, the most bandwidth

Recording rate capability vs. time

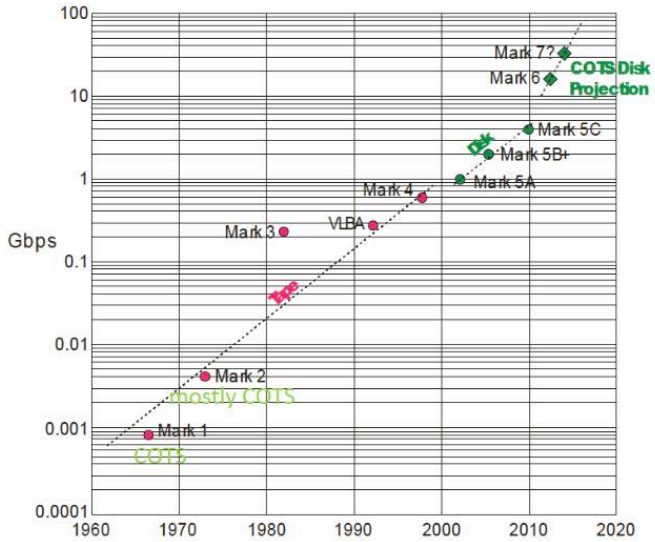

Event Horizon Telescope

MM VLBI Imaging of Sgr A*

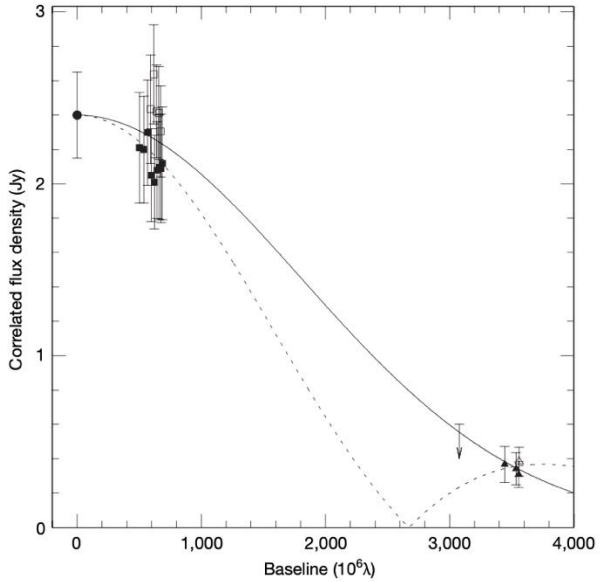

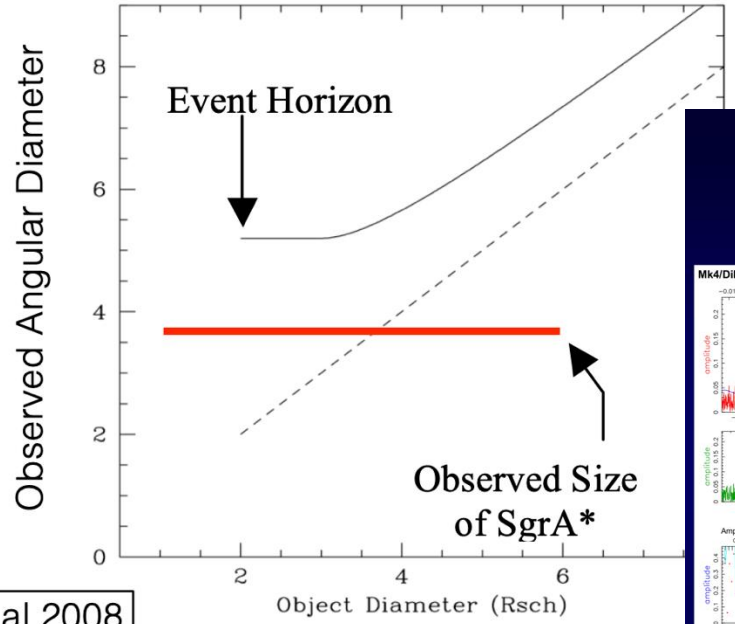

Doeleman et al 2008

First VLBI fringes with APEX at 230 GHz
(May 7, 2012)

3C279 and MK5C, DBE & DBBC, 1.92 Gbit/s, 480 MHz bandwidth

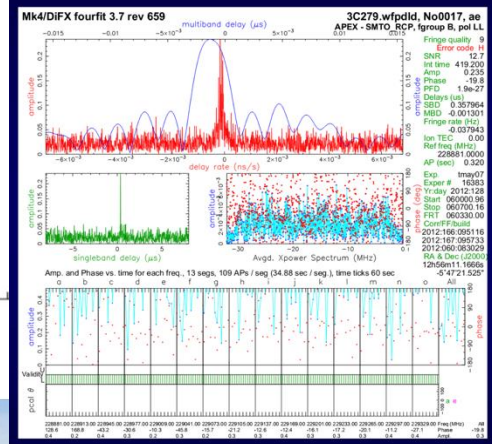

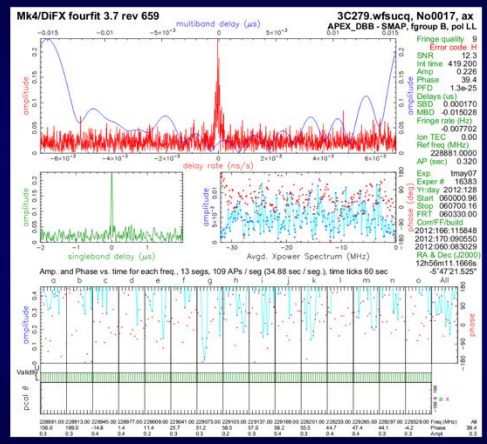

APEX – SMTO (Arizona): SNR 12.7

APEX – SMA (Hawaii): SNR 12.3

Courtesy of T. Krichbaum

Strong Evidence for a Black Hole

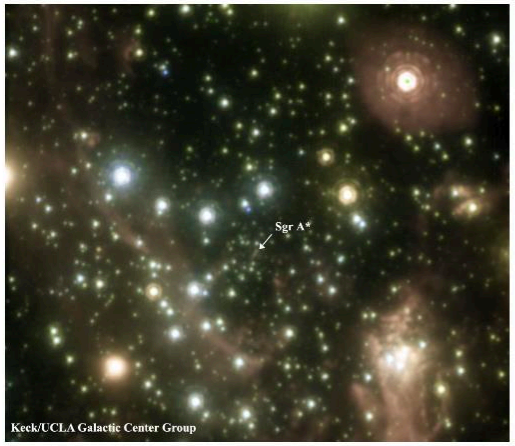

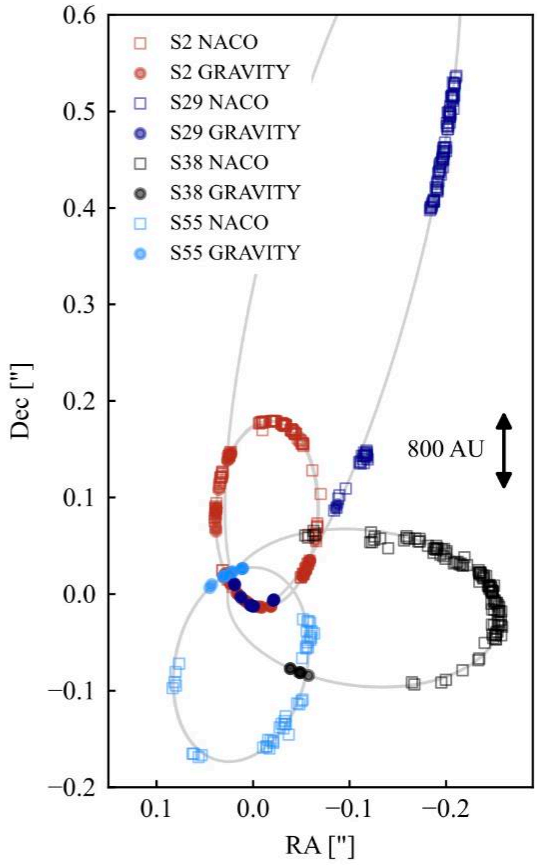

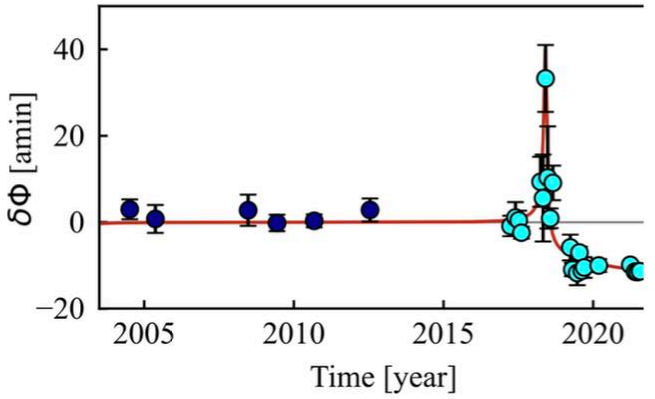

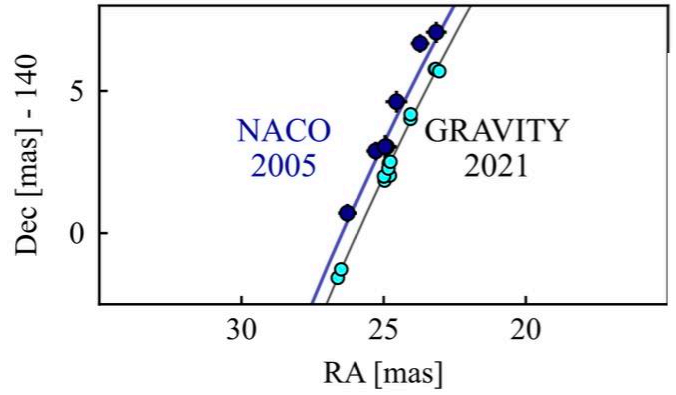

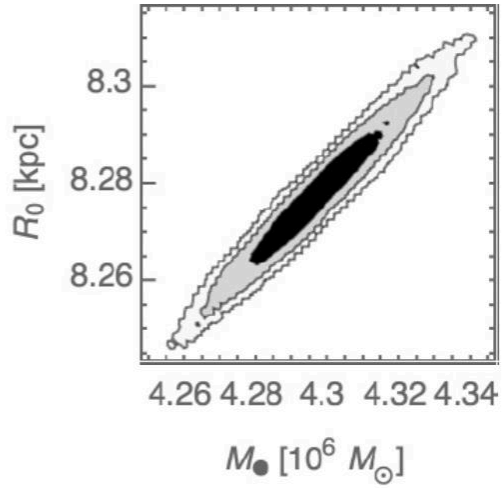

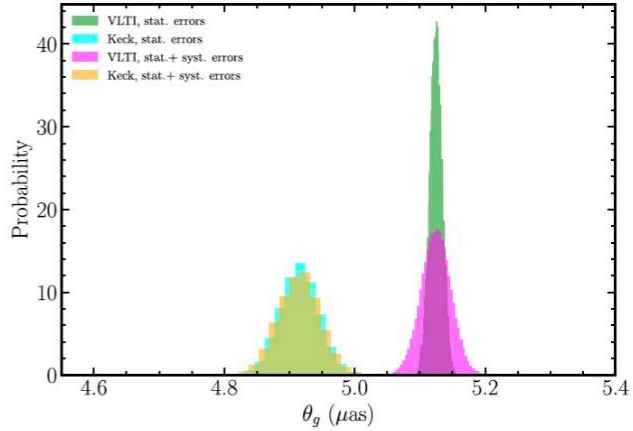

GRAVITY Collaboration 2022

Event Horizon Telescope

Event Horizon Telescope (EHT) : An Earth-sized telescope

Very long baseline interferometry : uses Earth rotation!

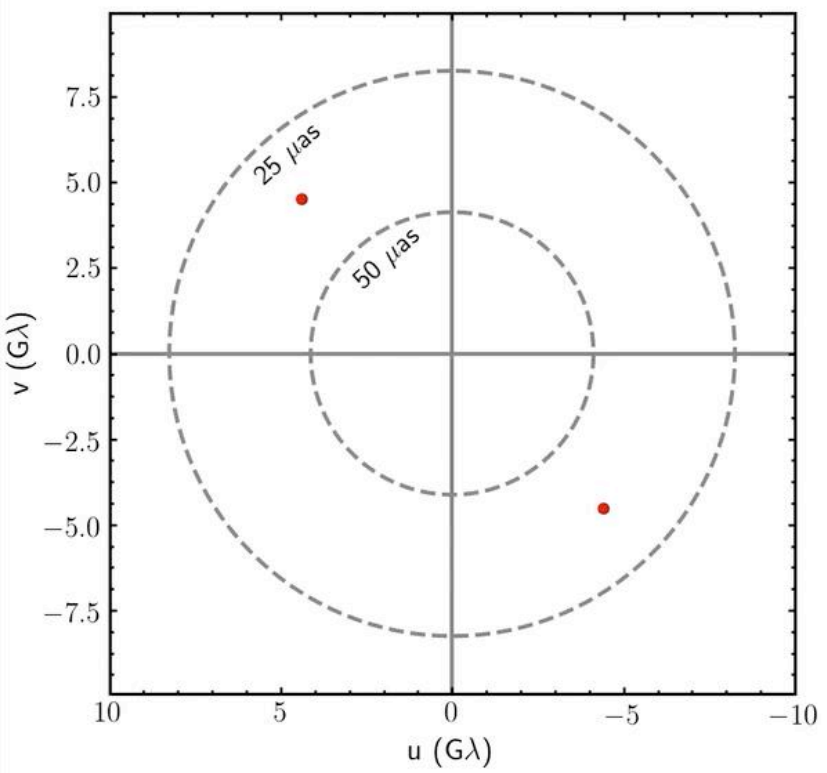

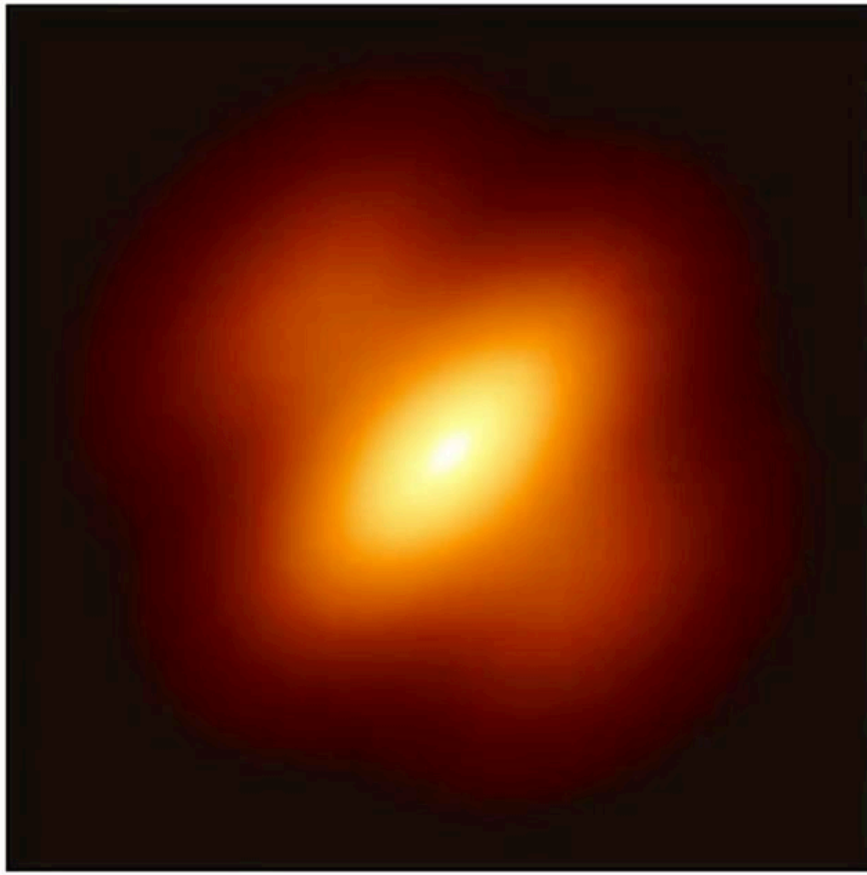

Slide & animation credit: Daniel Palumbo, Katie Bouman, Jonathan Weintroub, Maciek Wielgus

The EHT carries out yearly campaigns – there is a campaign ongoing now!!!!

- 8 facilities in 2017, 9 in 2018 (+GLT)
- 2021-2025: plus Kitt Peak and NOEMA array + KVN + GLT

- Each campaign ~2 week window and we observe ~7 days
- Multiwavelength coordination a challenge!

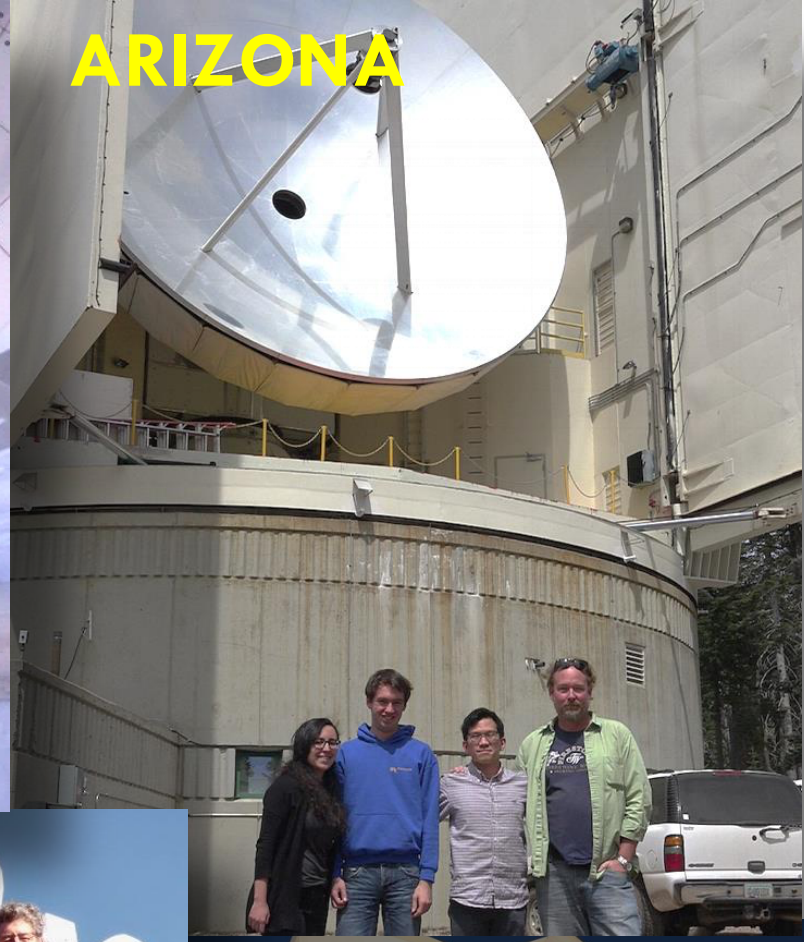

Slide courtesy Katie Bouman

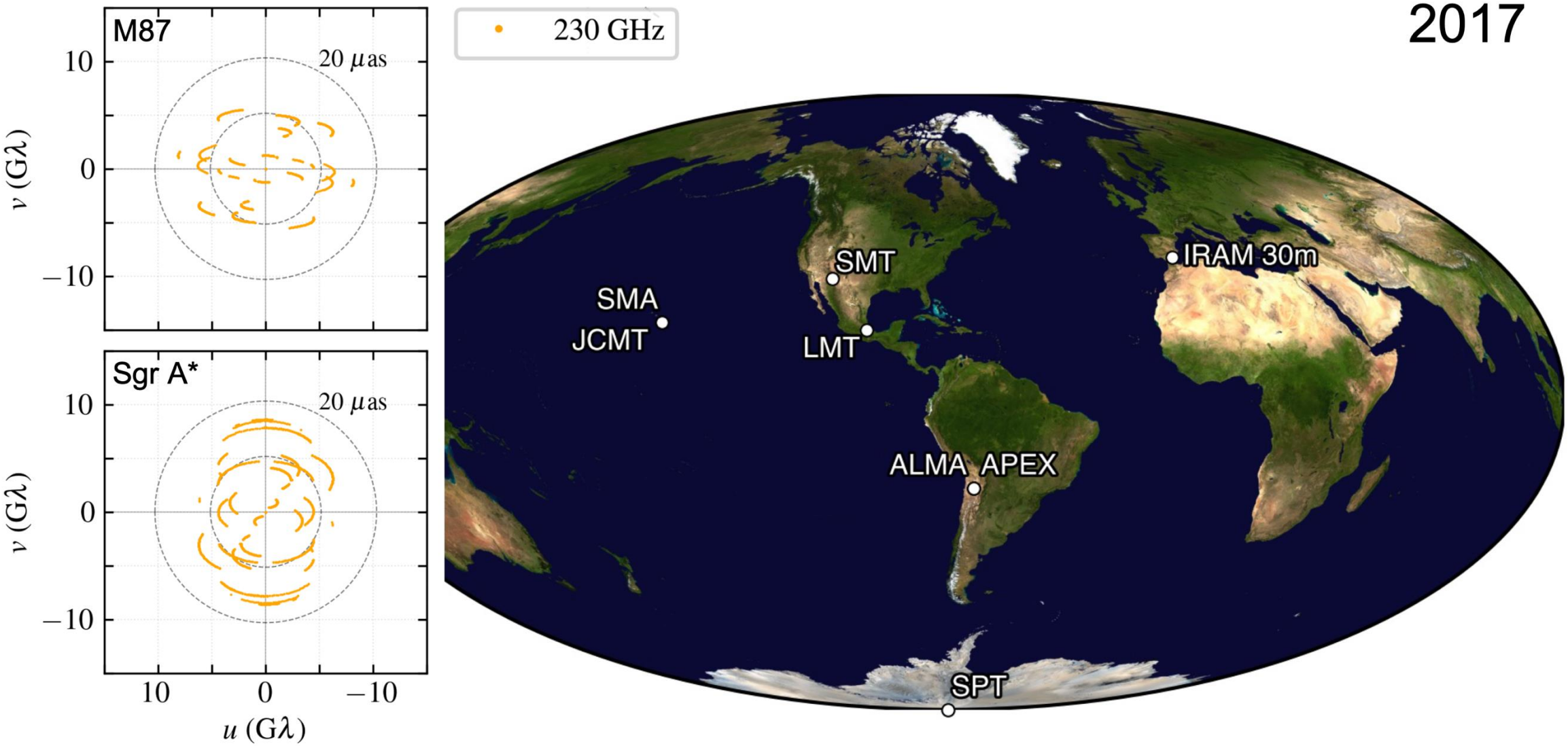
M87
20 μas
Sgr A*
20 μas
10
0
−10
ν (Gλ)
u (Gλ)
230 GHz
2017
SMA
JCMT
SMT
LMT
IRAM 30m
ALMA
APEX
SPT

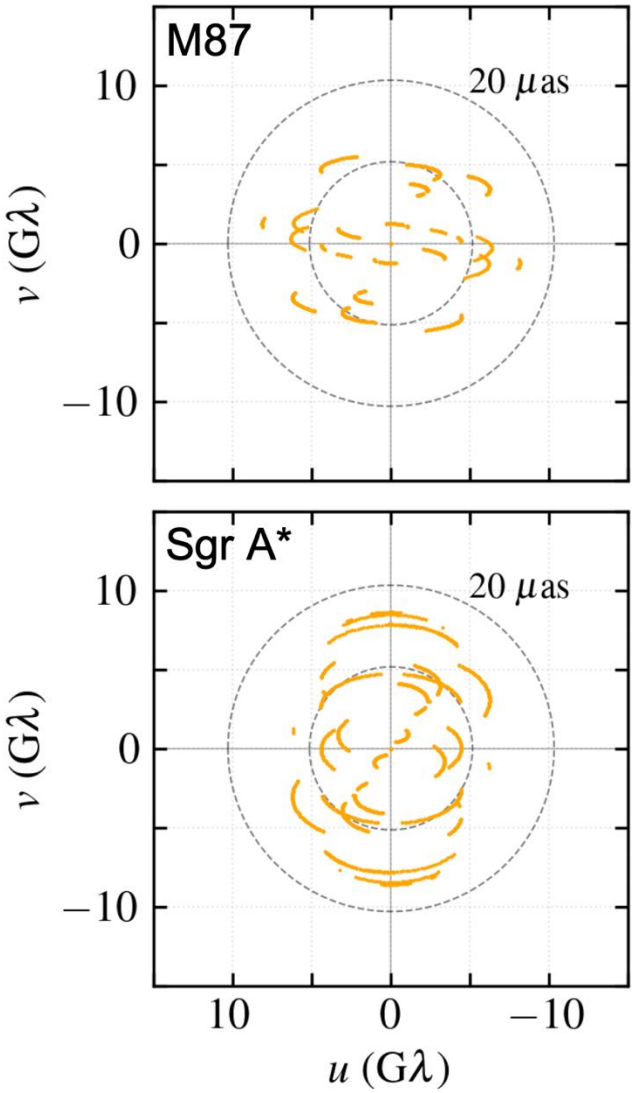
M87
20 μas
Sgr A*
20 μas
10
0
−10
ν (Gλ)
u (Gλ)

230 GHz

2017

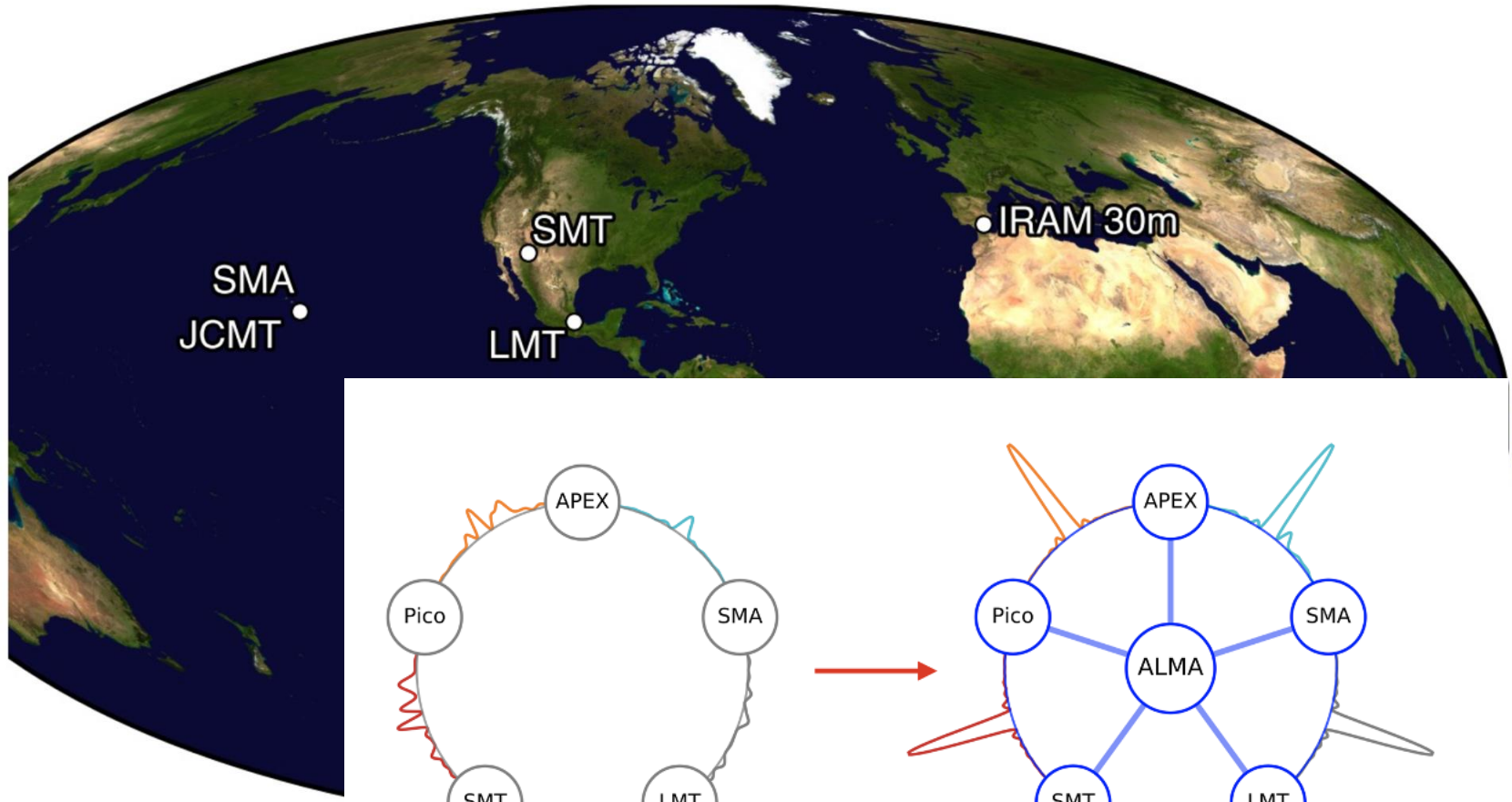
SMA
JCMT
SMT
LMT
IRAM 30m

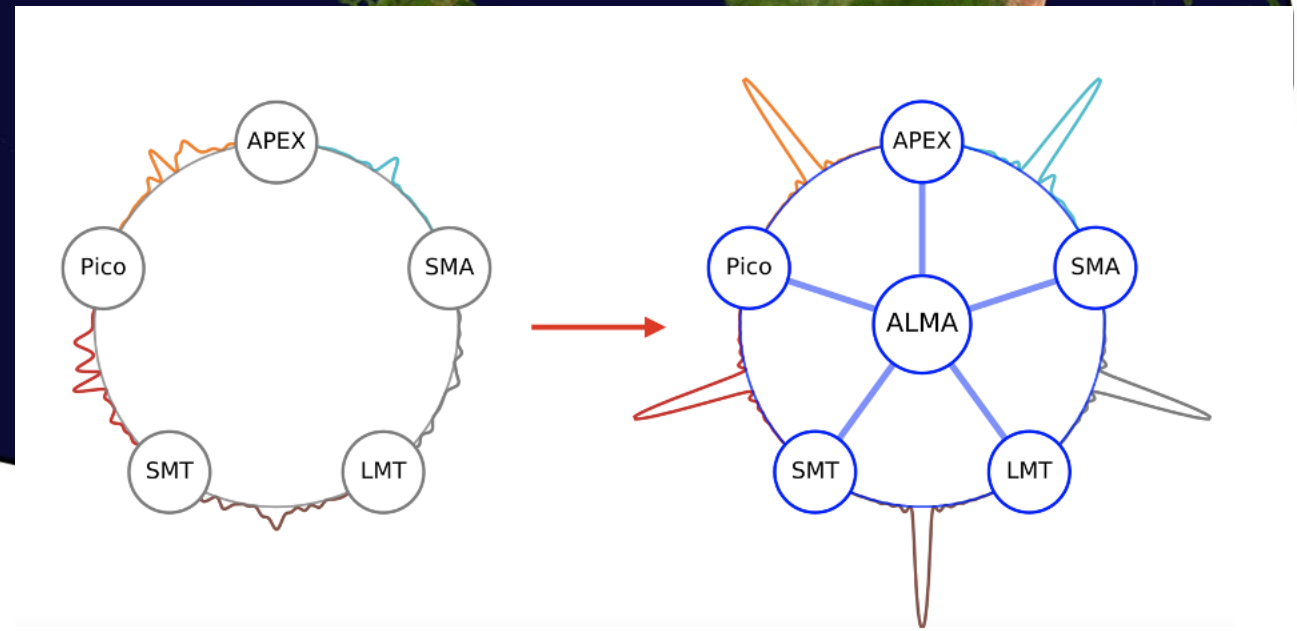
APEX
Pico
SMA
SMT
LMT
ALMA

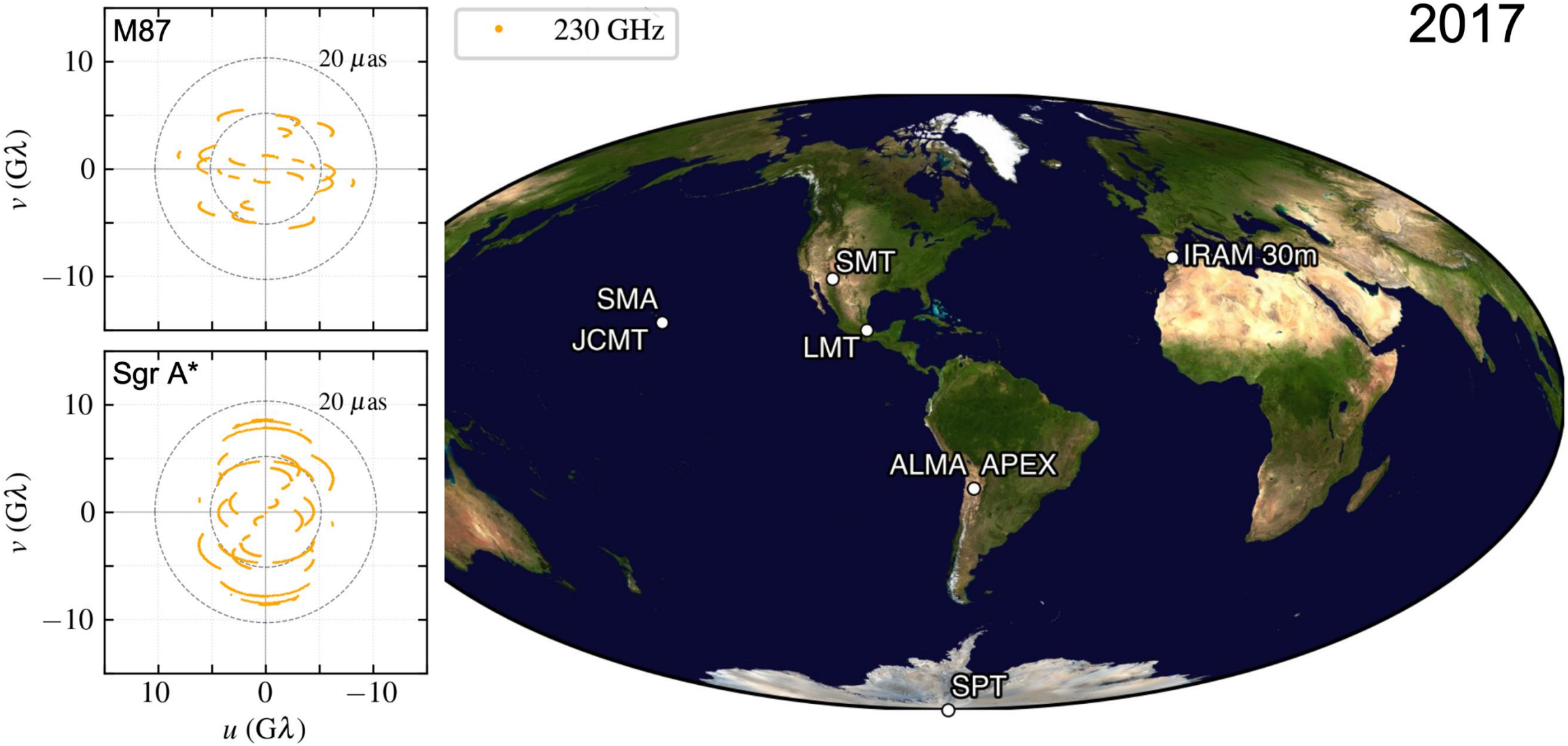
M87
20 μas
Sgr A*
20 μas
10
0
−10
ν (Gλ)
u (Gλ)
230 GHz
2017
SMA
JCMT
SMT
LMT
IRAM 30m
ALMA
APEX
SPT

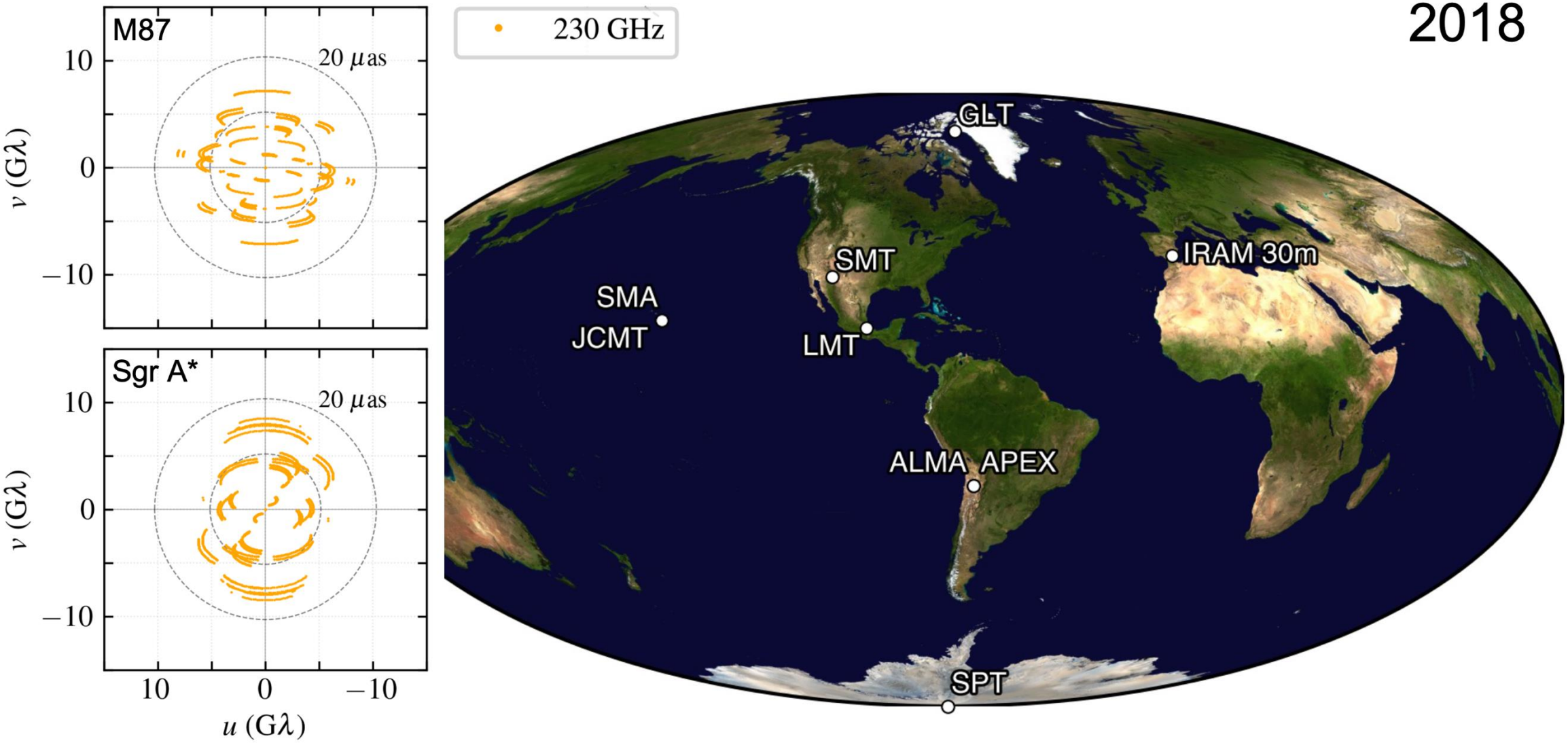
M87
20 μas
Sgr A*
20 μas
10
0
−10
ν (Gλ)
u (Gλ)
230 GHz
2018
GLT
SMT
IRAM 30m
SMA
JCMT
LMT
ALMA
APEX
SPT

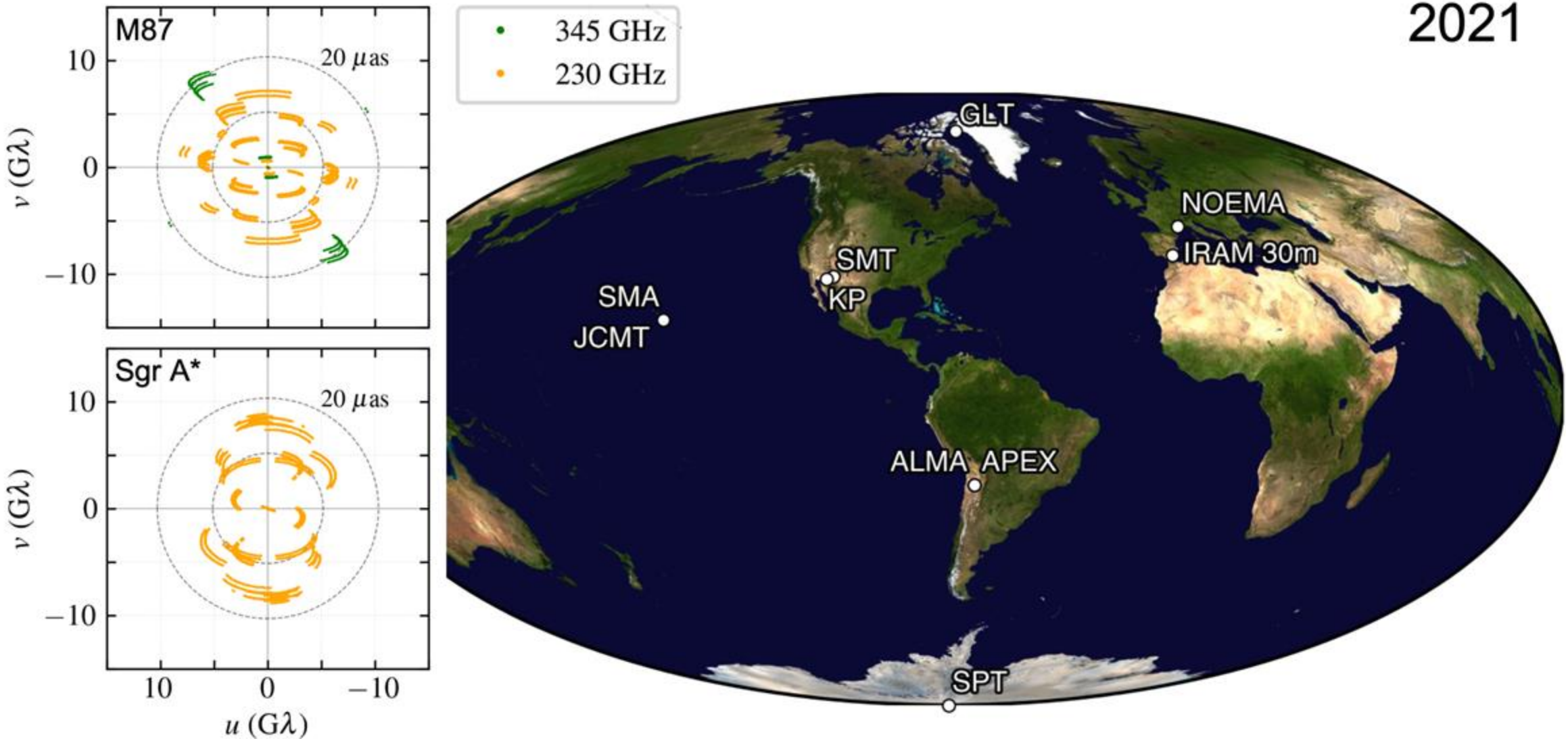
M87
20 μas
Sgr A*
20 μas
10
0
−10
ν (Gλ)
u (Gλ)
345 GHz
230 GHz
GLT
NOEMA
IRAM 30m
SMT
KP
SMA
JCMT
ALMA
APEX
SPT
2021

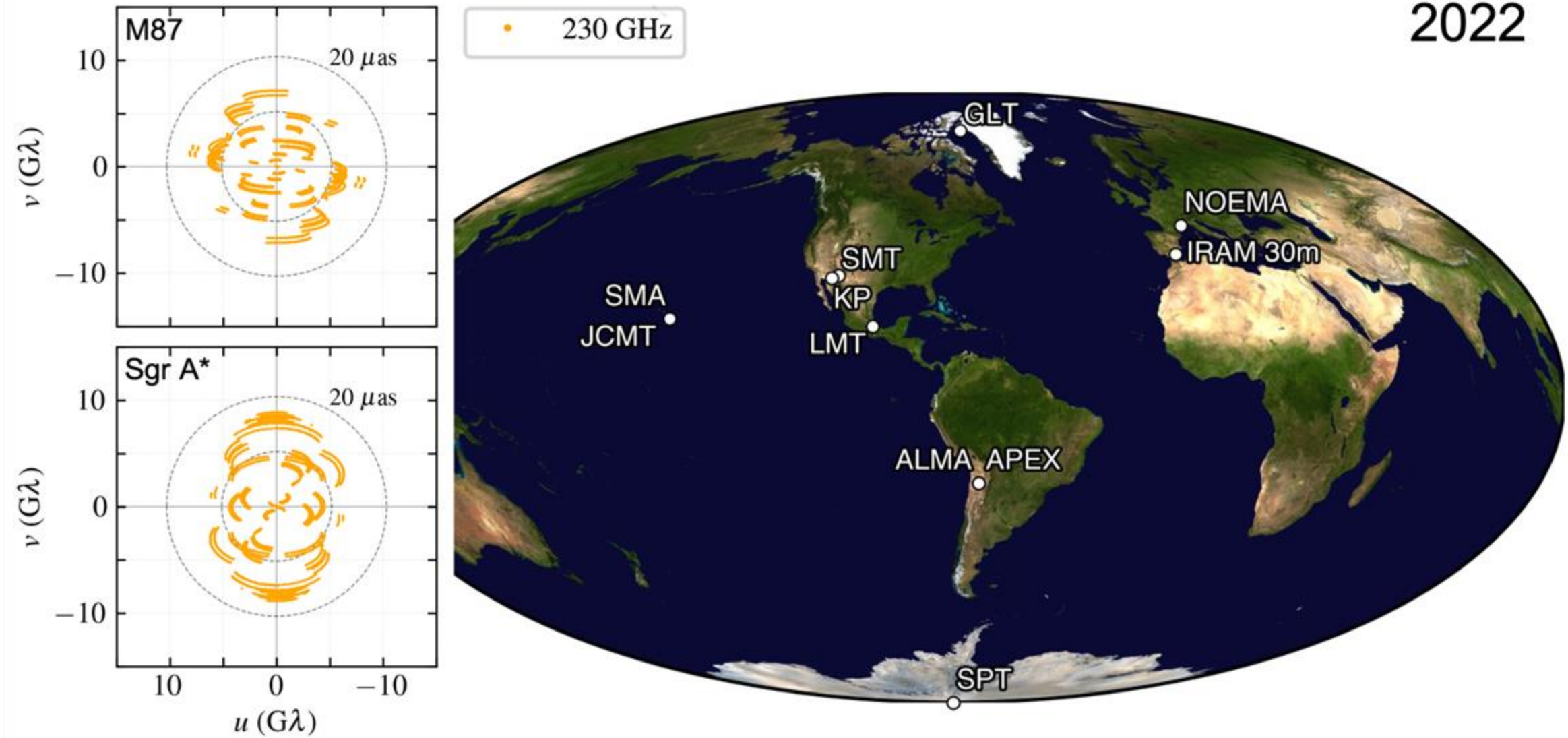
M87
20 μas
Sgr A*
20 μas
10
0
−10
v (Gλ)
u (Gλ)
230 GHz
2022
GLT
NOEMA
IRAM 30m
SMT
KP
LMT
SMA
JCMT
ALMA
APEX
SPT

2023

M87
Not observed

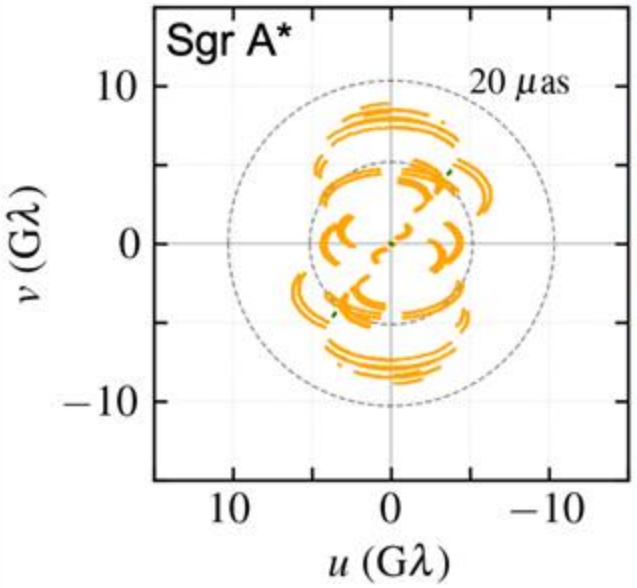

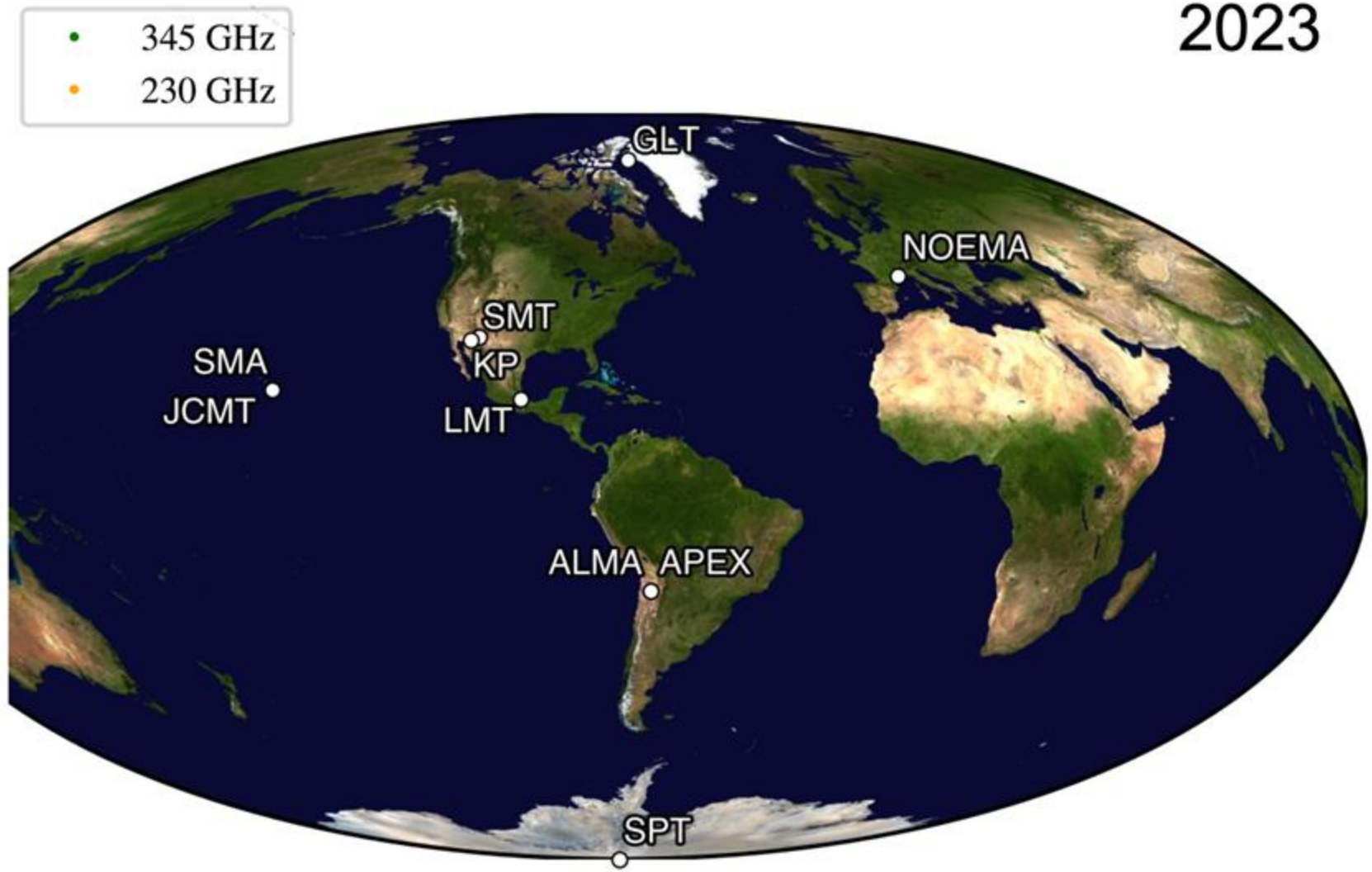

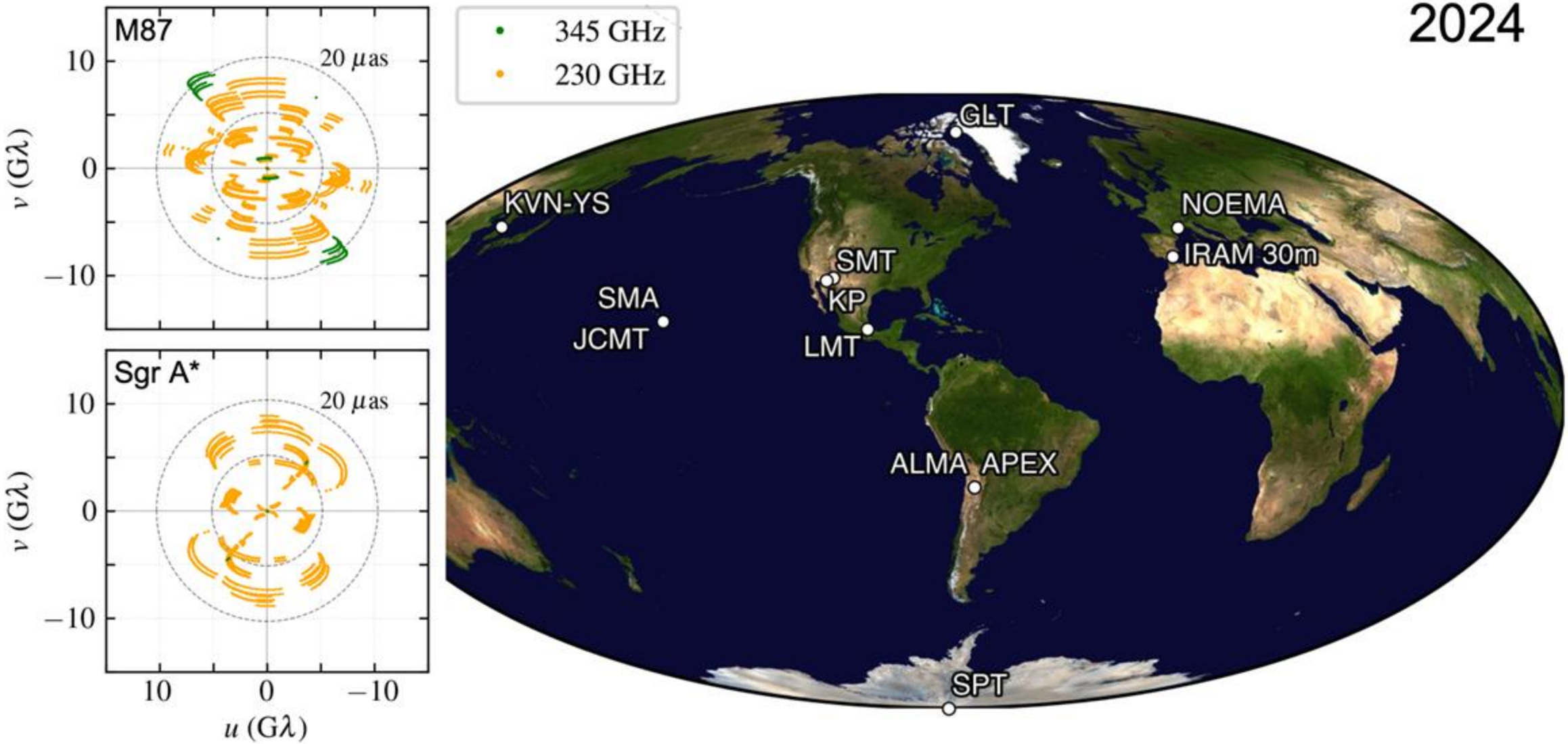
M87
20 μas
Sgr A*
20 μas
10
0
−10
ν (Gλ)
u (Gλ)
345 GHz
230 GHz
GLT
KVN-YS
NOEMA
IRAM 30m
SMT
KP
SMA
JCMT
LMT
ALMA
APEX
SPT
2024

The EHT campaigns

	<2017	2017	2018	2019/ 2020	2021	2022	2023
Stations	SMT, CARMA, SMA, JCMT APEX	SPT, ALMA, APEX, SMA, JCMT, LMT, SMT, PV	SPT, ALMA, APEX, SMA, JCMT, LMT, SMT, PV, GLT		SPT, ALMA, APEX, SMA, JCMT, SMT, PV, GLT, KP, NOEMA	SPT, ALMA, APEX, SMA, JCMT, LMT, SMT, PV, GLT, KP, NOEMA	SPT, ALMA, APEX, SMA, JCMT, LMT, SMT, GLT, KP, NOEMA
Bandwidth		32 Gbps	64 Gbps		64 Gbps	64 Gbps	64 Gbps
	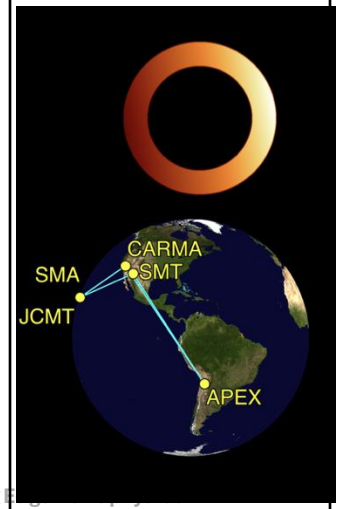 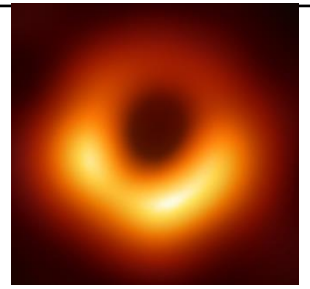 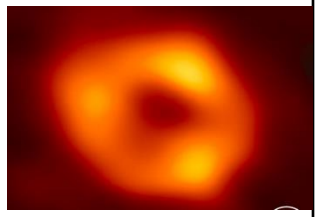 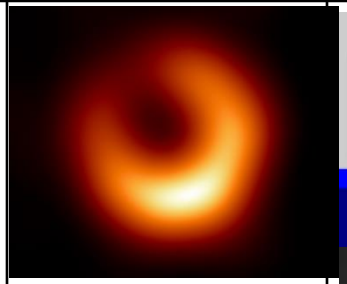 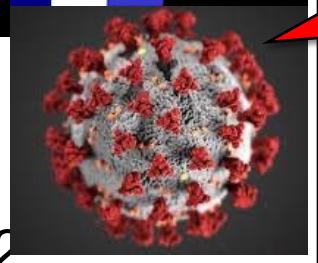 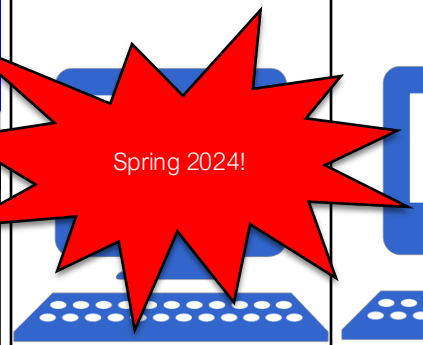 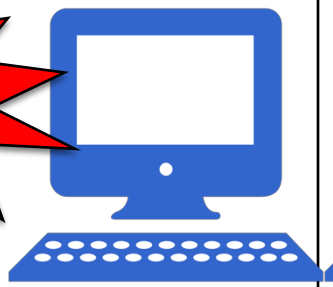					345 GHz

Essential to sample different accretion scales

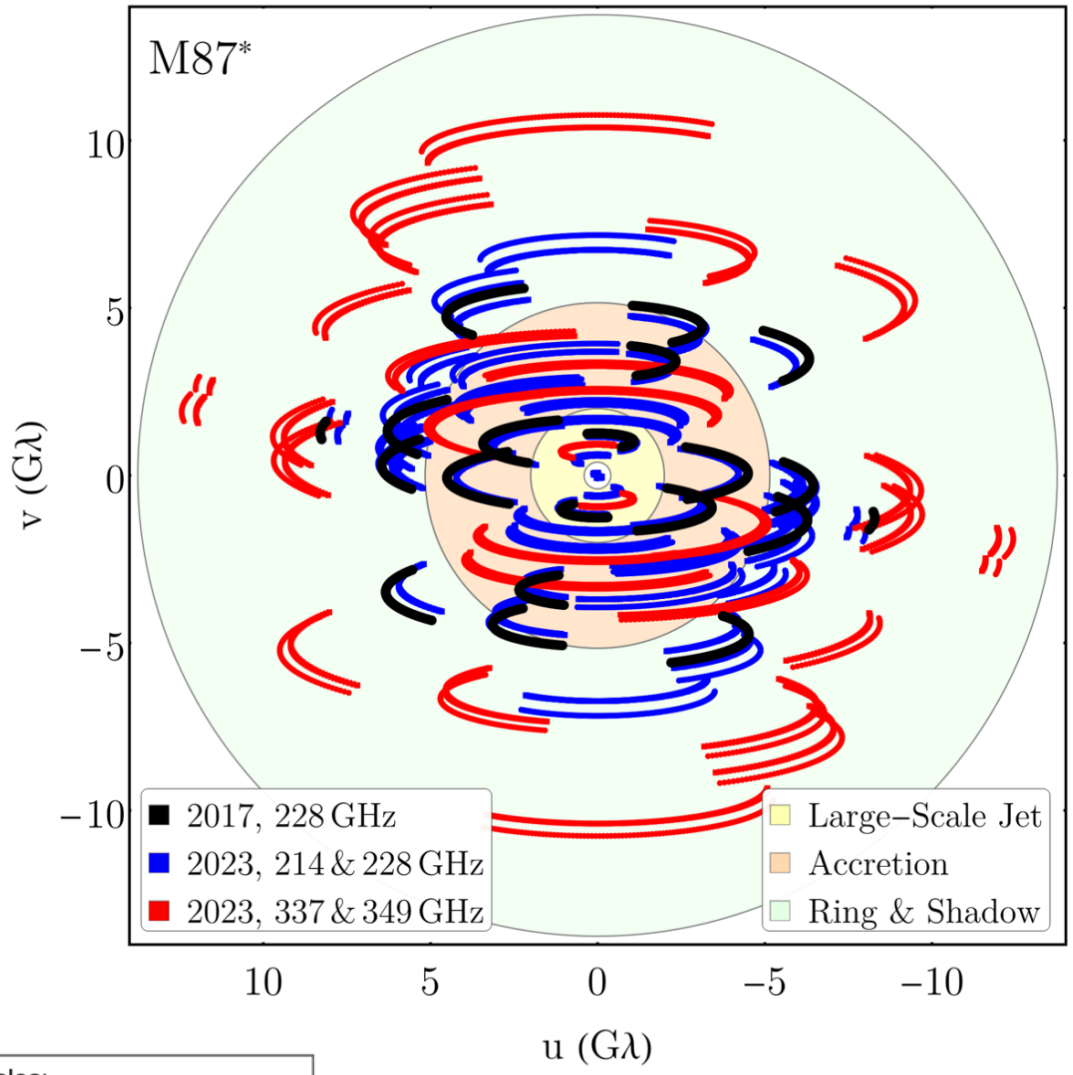

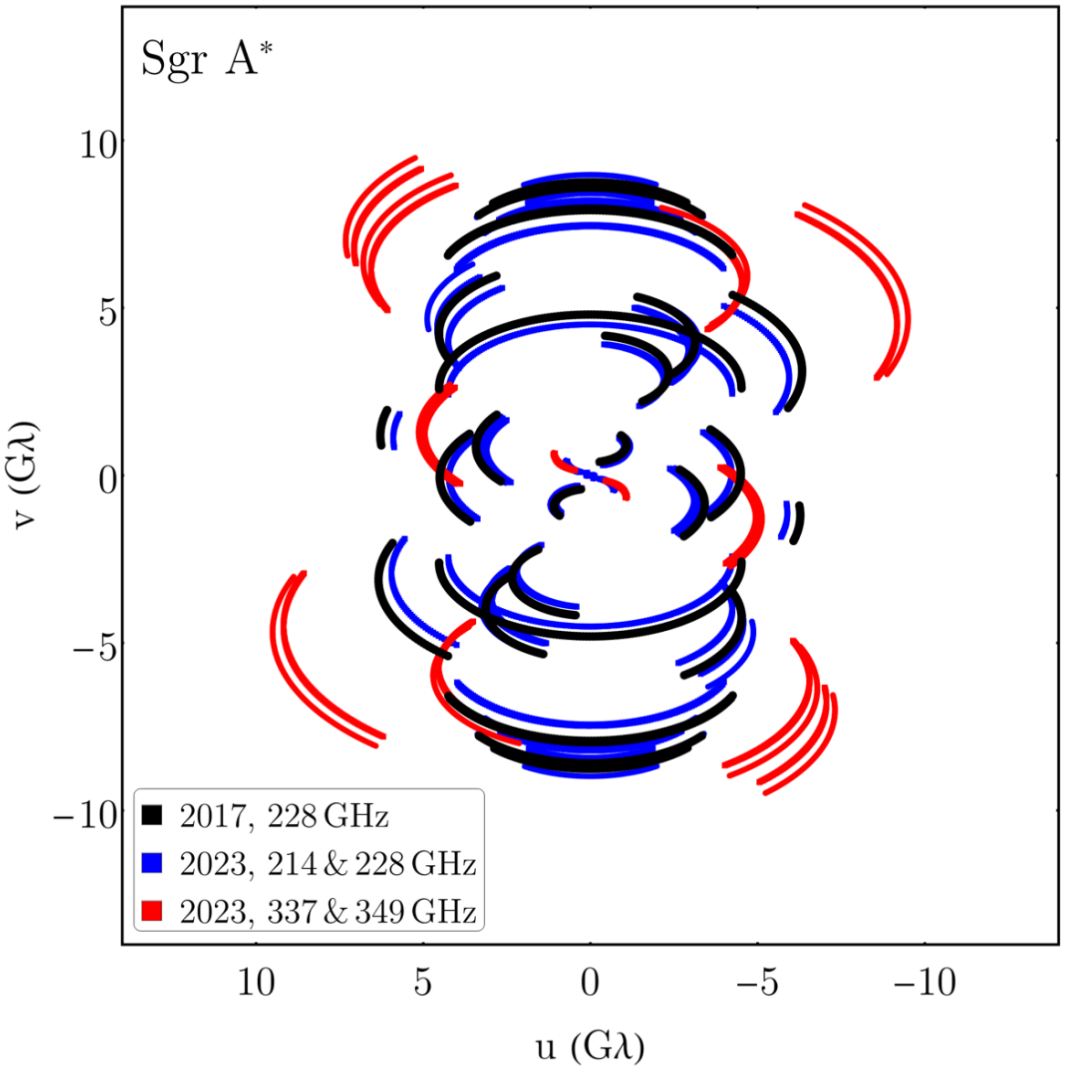

Angular Scales:
10 - 40 uas: Ring & Shadow
40 - 100 uas: Accretion & Jet Launch
100 - 500 uas: Large-Scale Jet

The Astrophysical Journal Letters, 875:L1 (17pp), 2019 April 10 https://doi.org/10.3847/2041-8213/ab0ec7
© 2019. The American Astronomical Society.
OPEN ACCESS

First M87 Event Horizon Telescope Results. I. The Shadow of the Supermassive Black Hole

The Event Horizon Telescope Collaboration
(See the end matter for the full list of authors.)
Received 2019 March 1; revised 2019 March 12; accepted 2019 March 12; published 2019 April 10

Abstract

When surrounded by a transparent emission region, black holes are expected to reveal a dark shadow caused by gravitational light bending and photon capture at the event horizon. To image and study this phenomenon, we have assembled the Event Horizon Telescope, a global very long baseline interferometry array observing at a wavelength of 1.3 mm. This allows us to reconstruct event-horizon-scale images of the supermassive black hole candidate in the center of the giant elliptical galaxy M87. We have resolved the central compact radio source as an asymmetric bright emission ring with a diameter of 42 ± 3 μas, which is circular and encompasses a central depression in brightness with a flux ratio $\gtrsim$10:1. The emission ring is recovered using different calibration and imaging schemes, with its diameter and width remaining stable over four different observations carried out in different days. Overall, the observed image is consistent with expectations for the shadow of a Kerr black hole as predicted by general relativity. The asymmetry in brightness in the ring can be explained in terms of relativistic beaming of the emission from a plasma rotating close to the speed of light around a black hole. We compare our images to an extensive library of ray-traced general-relativistic magnetohydrodynamic simulations of black holes and derive a central mass of $M = (6.5 \pm 0.7) \times 10^9\,M_\odot$. Our radio-wave observations thus provide powerful evidence for the
and as the central engines of active galactic nuclei. They a
limit and on a mass scale that was so far not accessible.

Key words: accretion, accretion disks – black hole phys
galaxies: jets – gravitation

1. Introduction

Black holes are a fundamental prediction of the theory of general relativity (GR; Einstein 1915). A defining feature of black holes is their event horizon, a one-way causal boundary in spacetime from which not even light can escape (Schwarzschild 1916). The production of black holes is generic in GR (Penrose 1965), and more than a century after Schwarzschild, they remain at the heart of fundamental questions in unifying GR with quantum physics (Hawking 1976; Giddings 2017).

Black holes are common in astrophysics and are found over a wide range of masses. Evidence for stellar-mass black holes comes from X-ray (Webster & Murdin 1972; Remillard & McClintock 2006) and gravitational-wave measurements (Abbott et al. 2016). Supermassive black holes, with masses from millions to tens of billions of solar masses, are thought to exist in the centers of nearly all galaxies (Lynden-Bell 1969; Kormendy & Richstone 1995; Miyoshi et al. 1995), including in the Galactic center (Eckart & Genzel 1997; Ghez et al. 1998; Gravity Collaboration et al. 2018a) and in the nucleus of the nearby elliptical galaxy M87 (Gebhardt et al. 2011; Walsh et al. 2013).

Active galactic nuclei (AGNs) are central bright regions that can outshine the entire stellar population of their host galaxy. Some of these objects, quasars, are the most luminous steady sources in the universe (Schmidt 1963; Sanders et al. 1989) and are thought to be powered by supermassive black holes accreting matter at very high rates through a geometrically thin,

Original content from this work may be used under the terms of the Creative Commons Attribution 3.0 licence. Any further distribution of this work must maintain attribution to the author(s) and the title of the work, journal citation and DOI.

maximum likelihood (RML; e.g., Narayan & Nityananda 1986; Wiaux et al. 2009; Thiébaut 2013). RML is a forward-modeling approach that searches for an image that is not only consistent with the observed data but also favors specified image properties (e.g., smoothness or compactness). As with CLEAN, RML methods typically iterate between imaging and self-calibration, although they can also be used to image directly on robust closure quantities immune to station-based calibration errors. RML methods have been extensively developed for the EHT (e.g., Honma et al. 2014; Bouman et al. 2016; Akiyama et al. 2017; Chael et al. 2018b; see also Paper IV).

Every imaging algorithm has a variety of free parameters that can significantly affect the final image. We adopted a two-stage imaging approach to control and evaluate biases in the reconstructions from our choices of these parameters. In the first stage, four teams worked independently to reconstruct the first EHT images of M87[*] using an early engineering data release. The teams worked without interaction to minimize shared bias, yet each produced an image with a similar prominent feature: a ring of diameter ~38–44 μas with enhanced brightness to the south (see Figure 4 in Paper IV).

In the second imaging stage, we developed three imaging pipelines, each using a different software package and associated methodology. Each pipeline surveyed a range of imaging parameters, producing between $\sim 10^3$ and 10^4 images from different parameter combinations. We determined a "Top-Set" of parameter combinations that both produced images of M87[*] that were consistent with the observed data and that reconstructed accurate images from synthetic data sets corresponding to four known geometric models (ring, crescent, filled disk, and asymmetric double source). For all pipelines, the Top-Set images showed an asymmetric ring with a diameter of ~40 μas, with differences arising primarily in the effective angular resolutions achieved by different methods.

For each pipeline, we determined the single combination of fiducial imaging parameters out of the Top-Set that performed best across all the synthetic data sets and for each associated imaging methodology (see Figure 11 in Paper IV). Because the angular resolutions of the reconstructed images vary among the pipelines, we blurred each image with a circular Gaussian to a common, conservative angular resolution of 20 μas. The top part of Figure 3 shows an image of M87[*] on April 11 obtained by averaging the three pipelines' blurred fiducial images. The image is dominated by a ring with an asymmetric azimuthal profile that is oriented at a position angle ~170° east of north. Although the measured position angle increases by ~20° between the first two days and the last two days, the image features are broadly consistent across the different imaging methods and across all four observing days. This is shown in the bottom part of Figure 3, which reports the images on different days (see also Figure 15 in Paper IV). These results are also consistent with those obtained from visibility-domain fitting of geometric and general-relativistic magnetohydrodynamics (GRMHD) models (Paper VI).

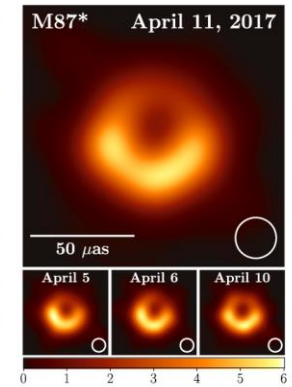

Figure 3. Top: EHT image of M87[*] from observations on 2017 April 11 as a representative example of the images collected in the 2017 campaign. The image is the average of three different imaging methods after convolving each with a circular Gaussian kernel to give matched resolutions. The largest of the three kernels (20 μas FWHM) is shown in the lower right. The image is shown in units of brightness temperature, $T_b = S\lambda^2/2k_B\Omega$, where S is the flux density, λ is the observing wavelength, k_B is the Boltzmann constant, and Ω is the solid angle of the resolution element. Bottom: similar images taken over different days showing the stability of the basic image structure and the equivalence among different days. North is up and east is to the left.

6. Theoretical Modeling

The appearance of M87[*] has been modeled successfully using GRMHD simulations, which describe a turbulent, hot, magnetized disk orbiting a Kerr black hole. They naturally produce a powerful jet and can explain the broadband spectral energy distribution observed in LLAGNs. At a wavelength of 1.3 mm, and as observed here, the simulations also predict a shadow and an asymmetric emission ring. The latter does not necessarily coincide with the innermost stable circular orbit, or ISCO, and is instead related to the lensed photon ring. To explore this scenario in great detail, we have built a library of synthetic images (Image Library) describing magnetized accretion flows onto black holes in GR[145] (Paper V). The images themselves are produced from a library of simulations (Simulation Library) collecting the results of four codes solving the equations of GRMHD (Gammie et al. 2003; Sądowski et al. 2014; Porth et al. 2017; Liska et al. 2018). The elements of the Simulation Library have been coupled to three different general-relativistic ray-tracing and radiative-transfer codes (GRRT, Bronzwaer et al. 2018; Mościbrodzka & Gammie 2018; Z. Younsi et al. 2019, in preparation). We limit ourselves to providing here a brief description of the initial setups and the physical scenarios explored in the simulations; see Paper V for details on both the GRMHD and GRRT codes, which have been cross-validated

[145] More exotic spacetimes, such as dilaton black holes, boson stars, and gravastars, have also been considered (Paper V).

The Astrophysical Journal Letters, 930:L12 (21pp), 2022 May 10 https://doi.org/10.3847/2041-8213/ac6674
© 2022. The Author(s). Published by the American Astronomical Society.
OPEN ACCESS

First Sagittarius A* Event Horizon Telescope Results. I. The Shadow of the Supermassive Black Hole in the Center of the Milky Way

The Event Horizon Telescope Collaboration
(See the end matter for the full list of authors.)
Received 2022 March 25; revised 2022 April 4; accepted 2022 April 8; published 2022 May 12

Abstract

We present the first Event Horizon Telescope (EHT) observations of Sagittarius A* (Sgr A*), the Galactic center source associated with a supermassive black hole. These observations were conducted in 2017 using a global interferometric array of eight telescopes operating at a wavelength of $\lambda = 1.3$ mm. The EHT data resolve a compact emission region with intrahour variability. A variety of imaging and modeling analyses all support an image that is dominated by a bright, thick ring with a diameter of 51.8 ± 2.3 μas (68% credible interval). The ring has modest azimuthal brightness asymmetry and a comparatively dim interior. Using a large suite of numerical simulations, we demonstrate that the EHT images of Sgr A* are consistent with the expected appearance of a Kerr black hole with mass $\sim 4 \times 10^6\,M_\odot$, which is inferred to exist at this location based on previous infrared observations of individual stellar orbits, as well as maser proper-motion studies. Our model comparisons disfavor scenarios w
nonspinning black holes and those with retrograde a
a supermassive black hole at the center of the M
dynamical measurements of stellar orbits on scale
variability. Furthermore, a comparison with the EH
with the predictions of general relativity spanning

Unified Astronomy Thesaurus concepts: Black h
Heterodyne interferometry (726); Galactic center

1. Introduction

Black holes are among the boldest and most prof
predictions of Einstein's theory of general relativity
Einstein 1915). Originally studied as a mathematical c
quence of GR rather than as physically relevant ob
(Schwarzschild 1916), they are now believed to be generic
sometimes inevitable outcomes of gravitational collapse (Op
heimer & Snyder 1939; Penrose 1965). In GR, the space
around astrophysical black holes is predicted to be uniq
described by the Kerr metric, which is entirely specified by
black hole's mass and angular momentum or "spin" (Kerr 1

The first empirical evidence for their existence was thr
stellar-mass black holes, beginning with observations of X
binary orbits (Bolton 1972; Webster & Murdin
McClintock & Remillard 1986) and culminating in
detection of gravitational waves from merging stellar-
black holes (Abbott et al. 2016). In parallel, the discovery
quasars are not stellar in nature but are rather extre
luminous, compact objects located in the centers of di
galaxies (Schmidt 1963) led to an intensive effort to ide
and measure the supermassive black holes (SMBHs) ene
tically favored to power them (Lynden-Bell 1969). Obse
tions now suggest that SMBHs not only lie at the cente
nearly every galaxy (Richstone et al. 1998) but also may p
role in their evolution (see, e.g., Magorrian et al.
Fabian 2012; Kormendy & Ho 2013), though how exactly

Original content from this work may be used under the
of the Creative Commons Attribution 4.0 licence. Any f
distribution of this work must maintain attribution to the author(s) and th
of the work, journal citation and DOI.

of the source. Moreover, at $\lambda = 1.3$ mm, Sgr A* has a compact flux density that is approximately four times larger than that of M87[*], with no appreciable contribution to the short-baseline visibilities from an extended jet. However, producing an image of Sgr A* requires additional assumptions because of the rapid source variability and interstellar scattering.

Specifically, VLBI imaging typically relies on Earth-rotation aperture synthesis, in which the projection of each baseline sweeps out an arc in the (u, v)-plane as the Earth rotates, allowing a sparse array of telescopes to obtain the (u, v)-coverage necessary for the imaging of a static source (Thompson et al. 2017). To account for the source structural variability, we used a parametric model discussed in Section 4. By incorporating this variability error budget, imaging and modeling methods designed for a static source can be applied to analyze data from a variable source.

To account for the interstellar scattering, we used two approaches (Paper III). The first, "on-sky imaging," applies no modifications to the data or images. In this approach, the algorithms simply reconstruct the scattered image of the source. The second, "descattered imaging," adds an error budget to interferometric visibilities to account for stochastic scattering substructure before deconvolving the ensemble-average scattering kernel. Both the ensemble-average kernel and the power spectrum of scattering are used (Psaltis et al. 2018), each of which is precisely known from an analysis combining decades of observations of Sgr A* at centimeter wavelengths (Johnson et al. 2018).

To test these imaging techniques and to select appropriate imaging parameters, we developed a suite of synthetic observations of seven geometric models that share the scattering and variability properties of Sgr A*. This suite included models with widely varying morphologies: rings, disks, a crescent, a double source, and a point-like source with an extended halo. Each model was selected to produce visibility amplitudes that were similar to those of Sgr A*, with two deep visibility minima, a physical scattering model applied, and stochastic temporal evolution generated by a statistical model (Lee & Gammie 2021).

We then selected the sets of imaging parameters that accurately reconstruct images across the entire test suite, including both ring and nonring data sets. These "top set" parameter choices yield a corresponding collection of reconstructed images of Sgr A* that provide both a representative average image and a measure of its uncertainty. In addition, we used a new Bayesian imaging method, which simultaneously estimates both the reconstructed image and its associated variability noise model (Broderick et al. 2020). This method does not require training on synthetic data, although we used the same test suite for comparison and validation of this method.

When applied to the Sgr A* data, over 95% of the top set images have a prominent ring morphology. For an analysis using the combination of April 6 and 7 data, all samples from the Bayesian imaging posterior show a ring morphology. In addition, geometric modeling of the EHT data shows a consistent statistical preference for ring morphologies over alternatives with comparable complexity. The ring has a diameter, width, and central brightness depression that are consistent across the different choices of imaging methods and parameters (see Paper III). However, the reconstructed images show diversity in their specific attributes, particularly the azimuthal intensity distribution around the ring. This uncertainty is a consequence of the limited EHT baseline coverage, compounded by the challenges of imaging a variable source. We categorized the reconstructed images into four clusters spanning the primary reconstructed structures: three clusters are ring modes with varying position angle, while the fourth is a comparatively small set of reconstructed images with diverse nonring morphologies. Figure 3 shows a representative average image of Sgr A* on April 7, as well as the average image for each of these clusters along with their relative occurrence frequency.

To quantify the ring parameters in a complementary way, we used several geometrical modeling methods, the parameterizations of which were guided by the reconstructed images of Sgr A*. These models are defined by a thick ring with azimuthal variations determined by low-order Fourier coefficients and an additional Gaussian brightness floor. Because these simple geometric models have a small number of parameters, they can be constrained using instantaneous

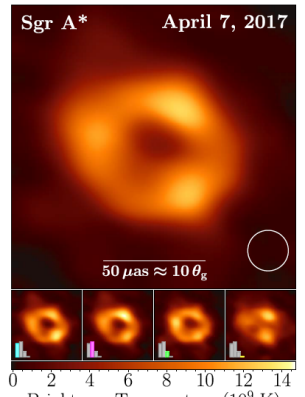

Figure 3. Representative EHT image of Sgr A* from observations on 2017 April 7. This image is an average over different reconstruction methodologies (CLEAN, RML, and Bayesian) and reconstructed morphologies. Color denotes the specific intensity, shown in units of brightness temperature. The inset circle shows the restoring beam used for CLEAN image reconstructions (20 μas FWHM). The bottom panels show average images within subsets with similar morphologies, with their prevalence indicated by the inset bars. The multiplicity of image modes reflects uncertainty due to the sparse baseline coverage; it does not correspond to different snapshots of the variable source. Nearly all reconstructed images show a prominent ring morphology. While the diameter and thickness of the ring are generally consistent across the reconstructions, the azimuthal structure of the ring is poorly constrained.

EHT results: **magnetically arrested disks**

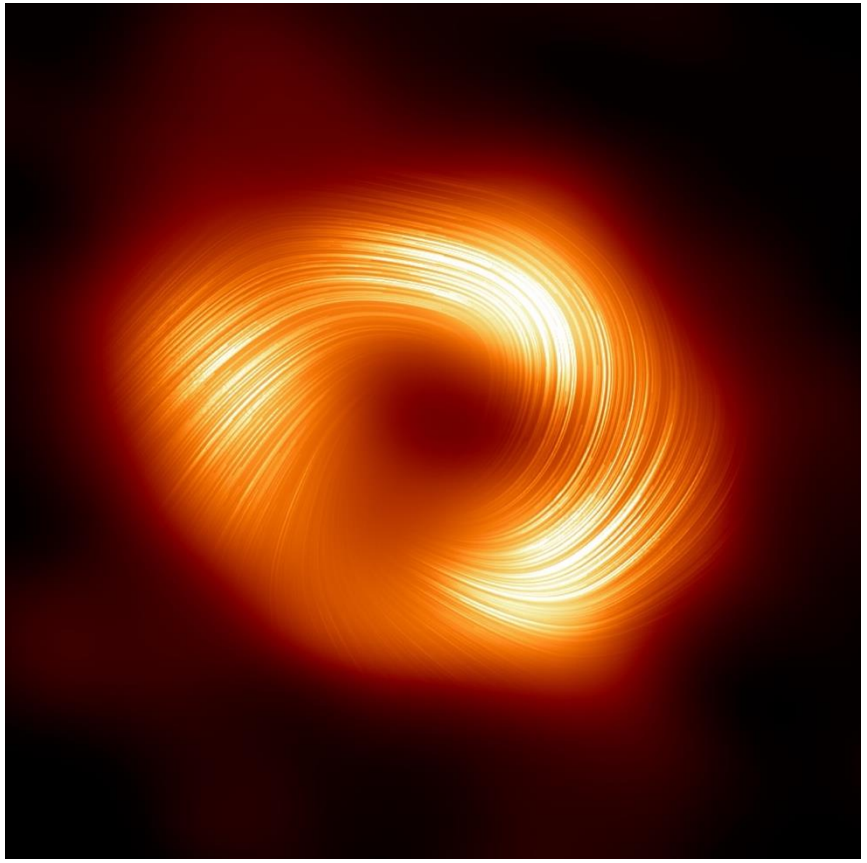

Total intensity (EHTC **Sgr A*** 2017 I, V)
Polarization (EHTC **Sgr A*** 2017 VIII)

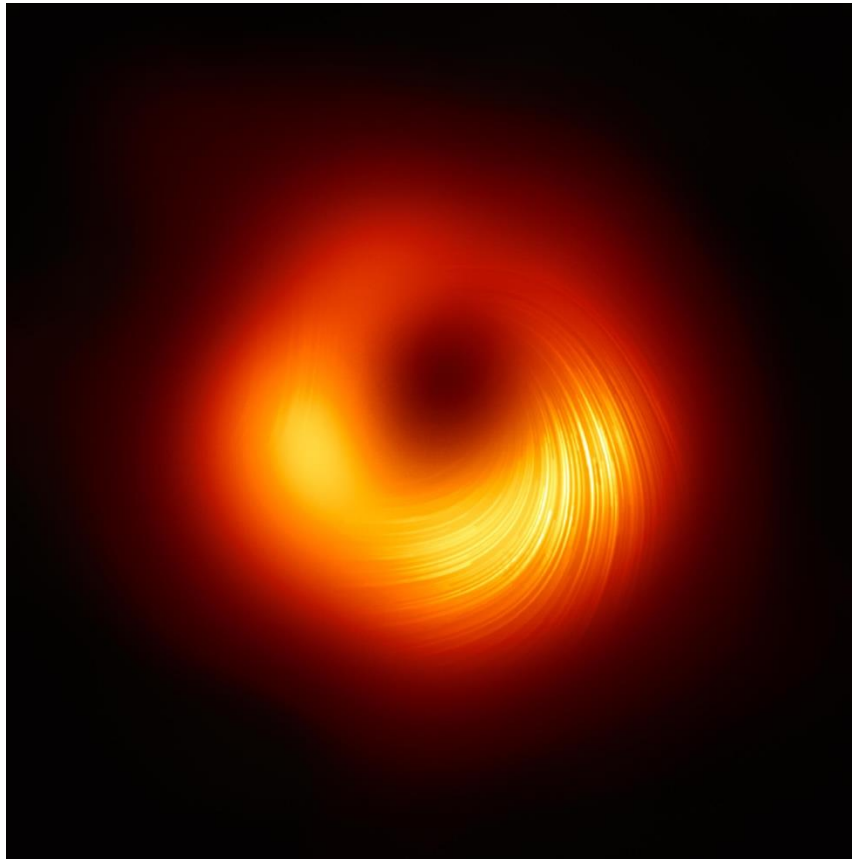

Total intensity (EHTC **M87** 2017 I, V)
Linear polarization (EHTC **M87** 2017 VIII)
Circular polarization (EHTC **M87** 2017 IX)
Total intensity (EHTC **M87** 2018 I, II)

- Shadow size and appearance of the rings consistent with General Relativity

  (EHTC **Sgr A*** **M87** 2017 VI)
- MAD models are favored
- Consisten with predictions from GR within < 10-17%

Multiwavelength campaigns

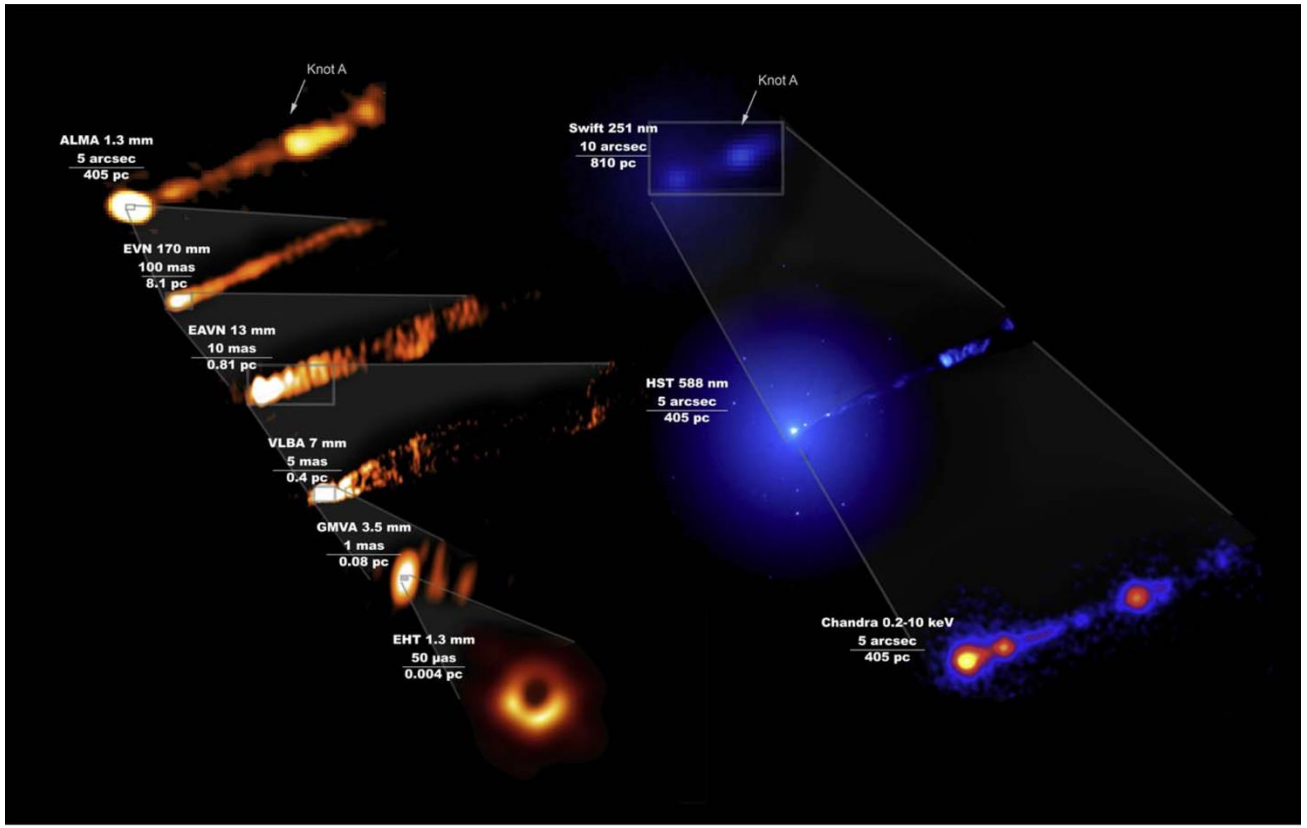

Algaba et al. 2021

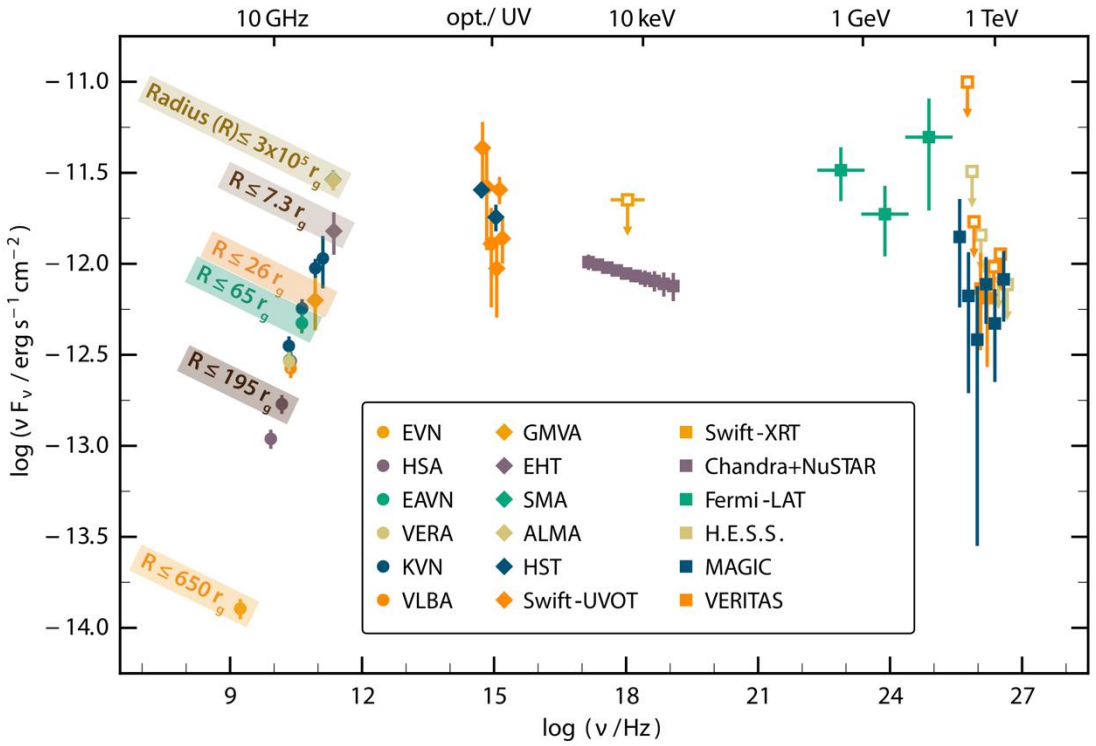

Source	Year	Day	Freq	ALMA	APEX	LMT	SMT	PV	SMA	JCMT	SPT	GLT	NOEMA	KP	Sites	Data	MWL Notes
M87*	2017	April 5	228	x	x	x	x	x	x	x	-	-	-	-	5 (7)	L2	EVN, EAVN, VLBA, GMVA, KVN, HST, Swift, Chandra, NuSTAR, Fermi, HESS, MAGIC VERITAS.
		April 6	228	x	x	x	x	x	x	x	-	-	-	-	5 (7)	L2	
		April 10	228	x	x	x	x	x	x	x	-	-	-	-	5 (7)	L2	Nucleus in low state.
		April 11	228	x	x	x	x	x	x	x	-	-	-	-	5 (7)	L2	

More than two black holes...

3C279

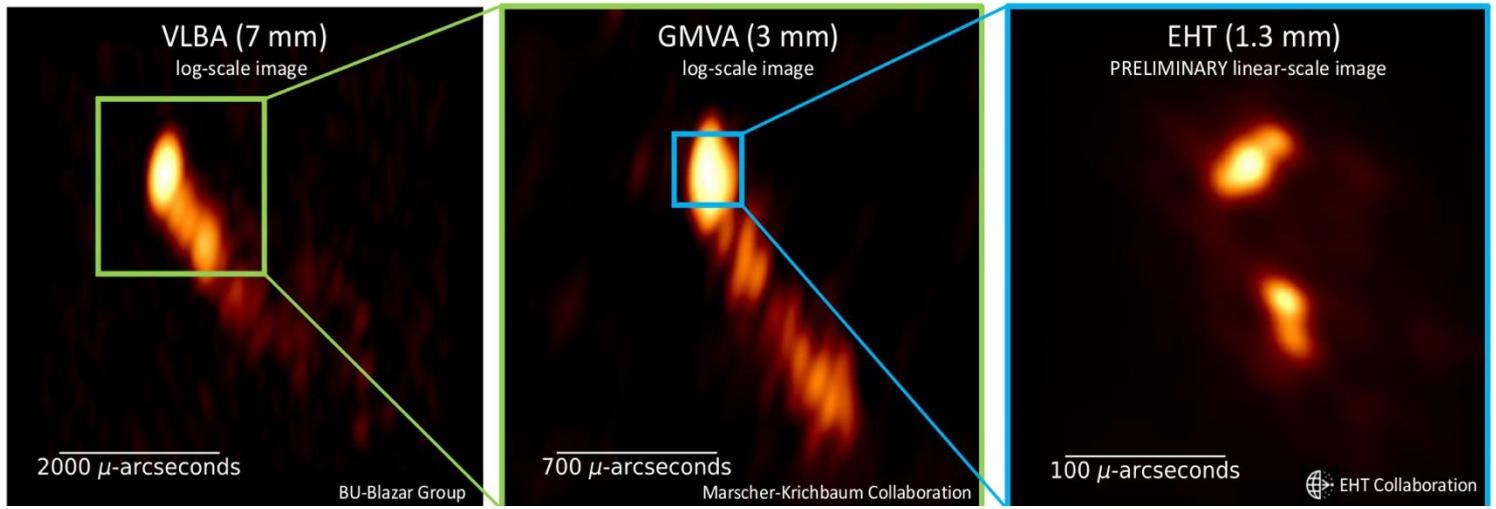

Jorstad et al. 2017 ; Kim et al. 2023

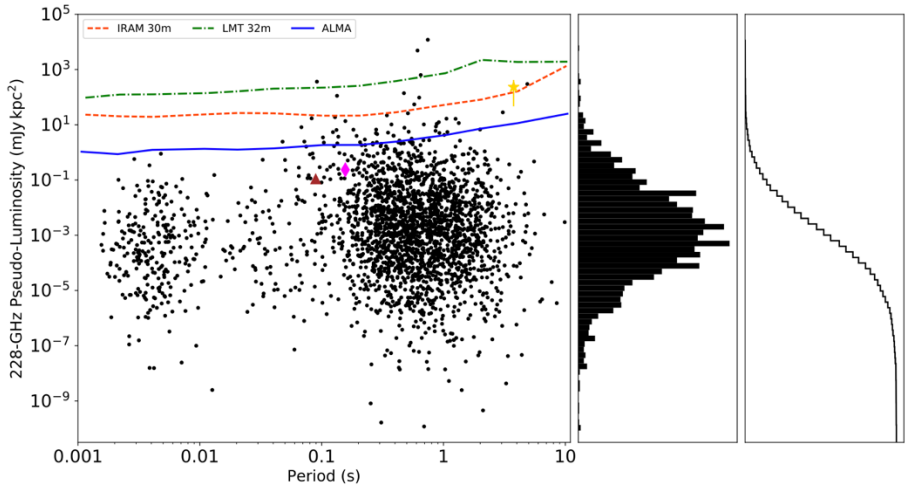

GC Pulsars, Torne et al. 2023

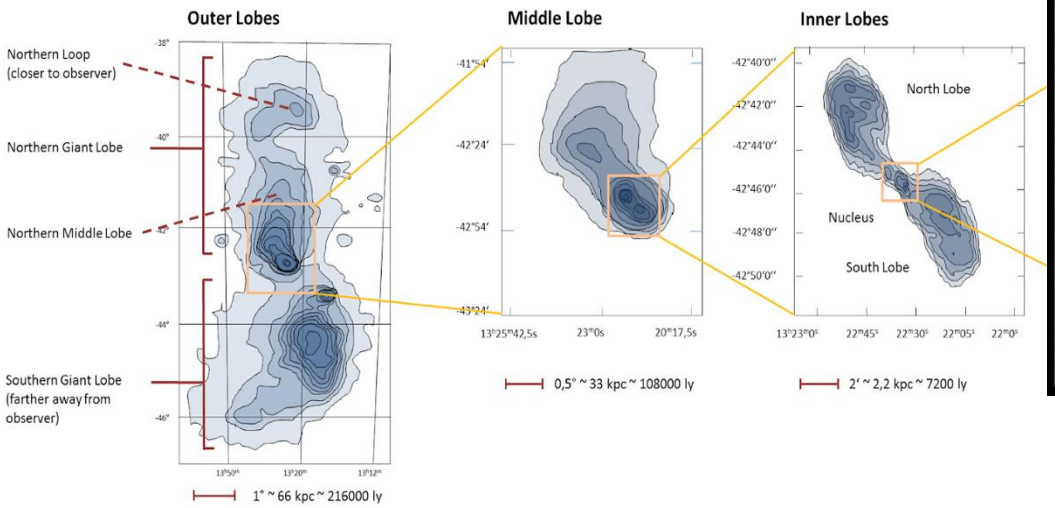

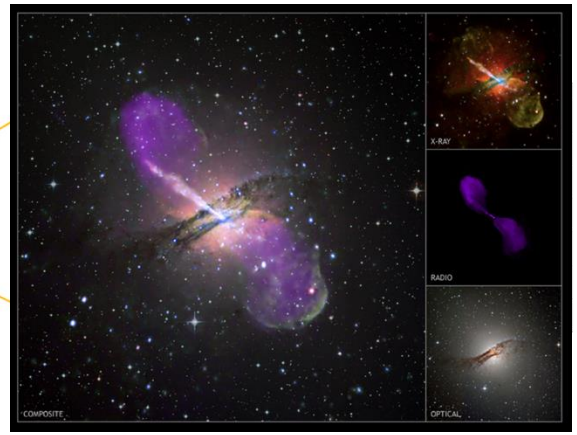

Centarus A

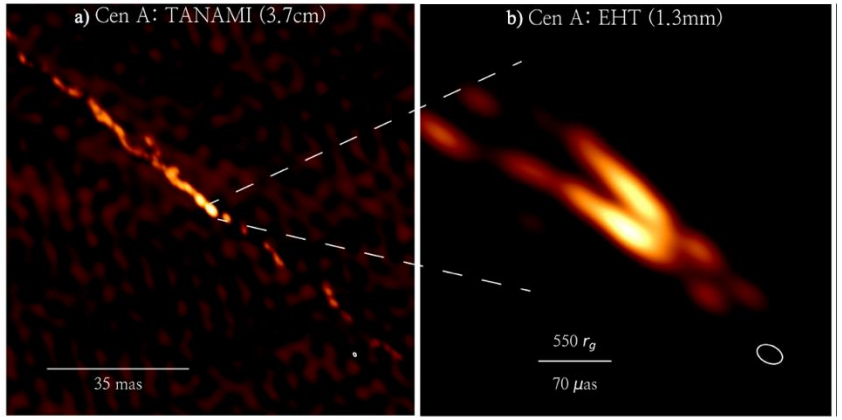

Jansen et al. 2021

More than two black h

3C279

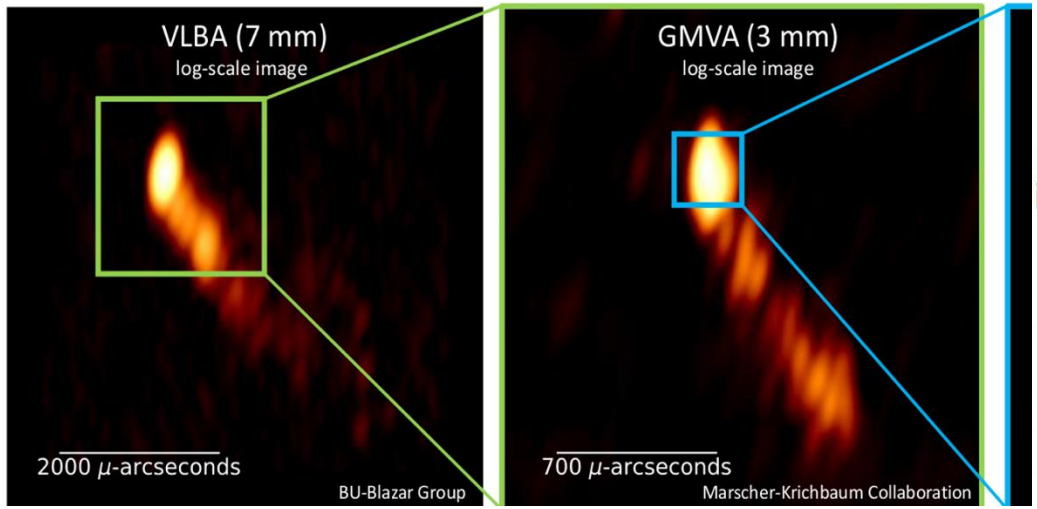

Jorstad et al. 2017 ; Kim et al. 2023

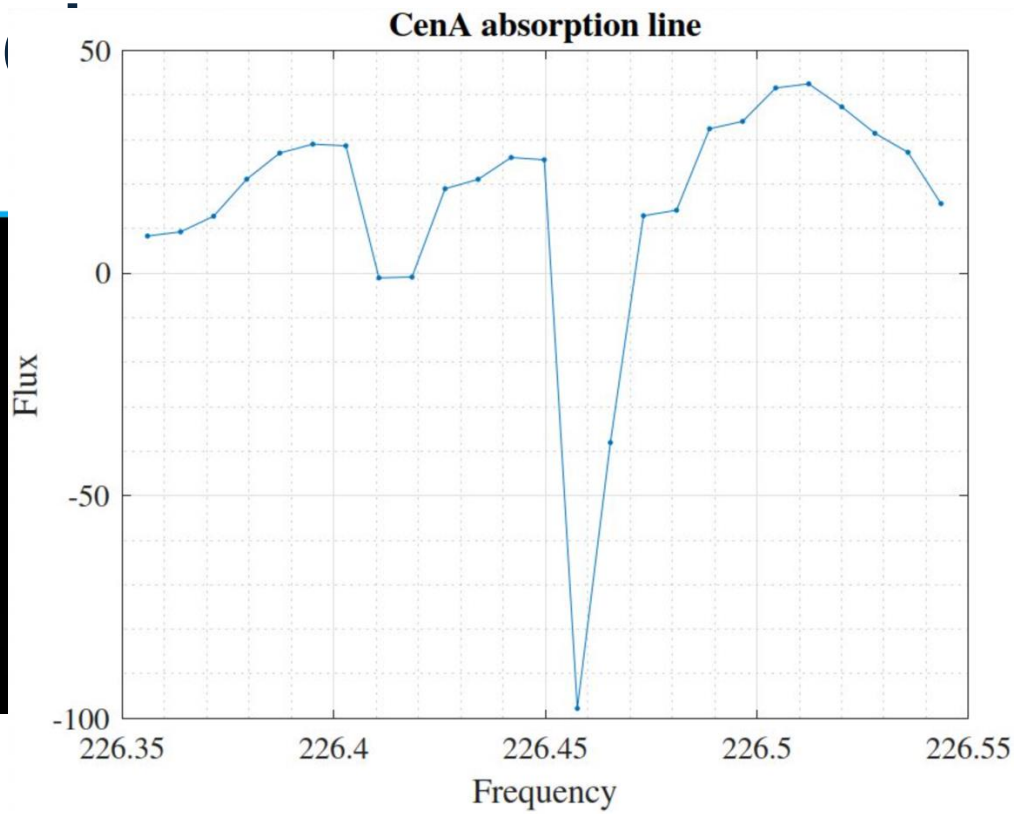

Ramakrishnan, Impellizzeri et al in prep

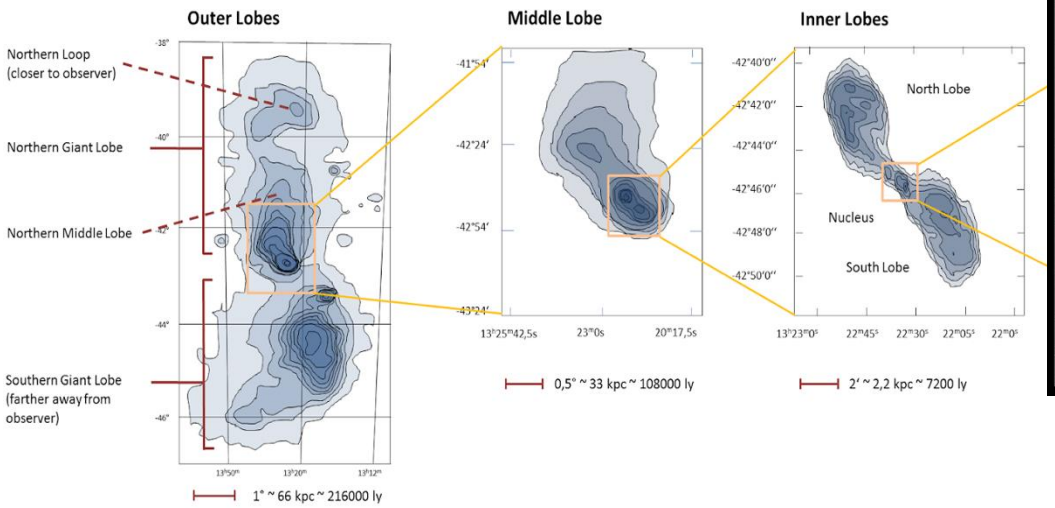

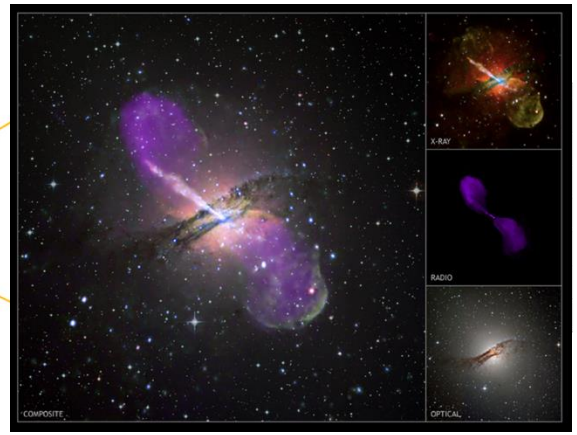

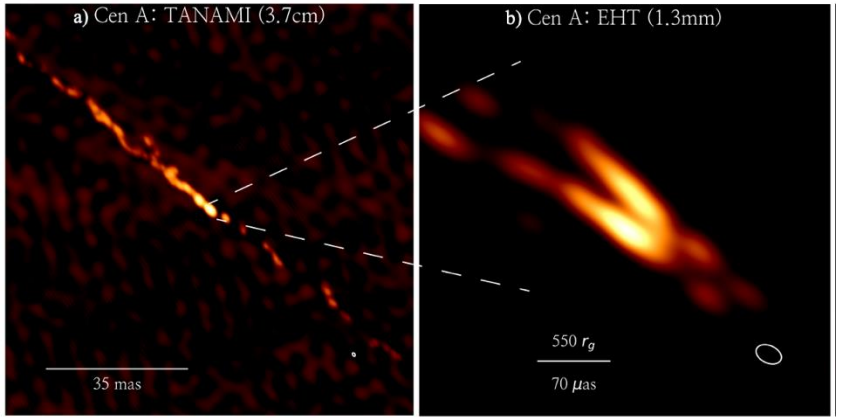

Centarus A

Jansen et al. 2021

The future is AGN-rich

Estimated jet-base EHT flux (0.1-mas-scale) vs BH ring size (i.e.10.4 Rg) for ETHER galaxies.

Targets observed with:
- EHT
- 86 GHz VLBI
- 43 GHz VLBI
- < 43 GHz VLBI (Ramakrishnan+2023)

SMBH mass is a:
- ● Measurement
- ▲ Estimate
- ■ WISE-based estimate

Targets in which:
- SMBH Shadow
- SMBH Spin
- SMBH Mass could be resolved with ground ngEHT (Phase 1) (Johnson+2023, Pesce+2022)

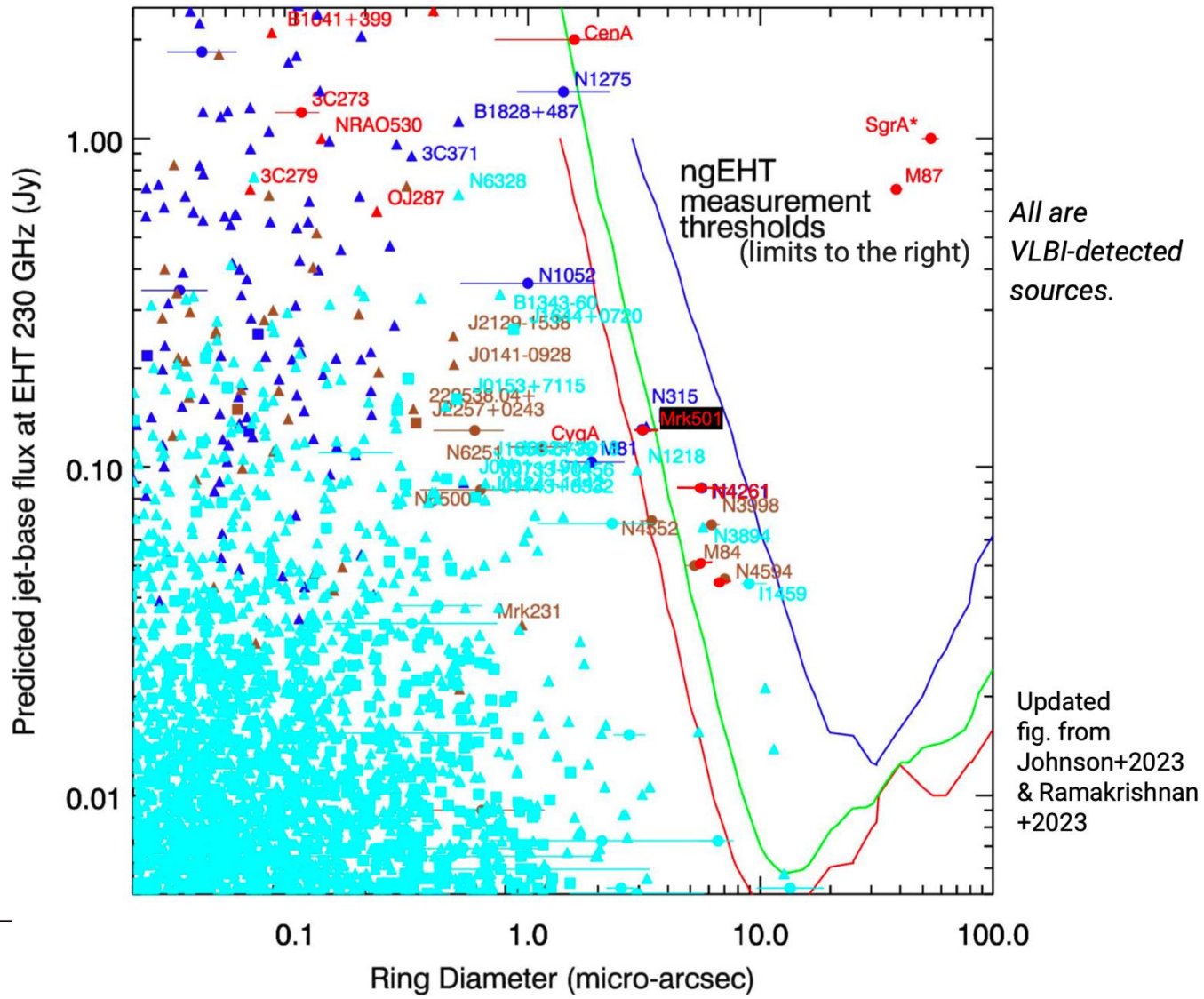

Ramkrishnan et al. 2023

Figure: Dhanya Nair

Primary EHT Results

- Black holes power active galactic nuclei
- EHT GR tests of BHs span 3 orders of magnitude
- Precision measurements of accretion and jet physics

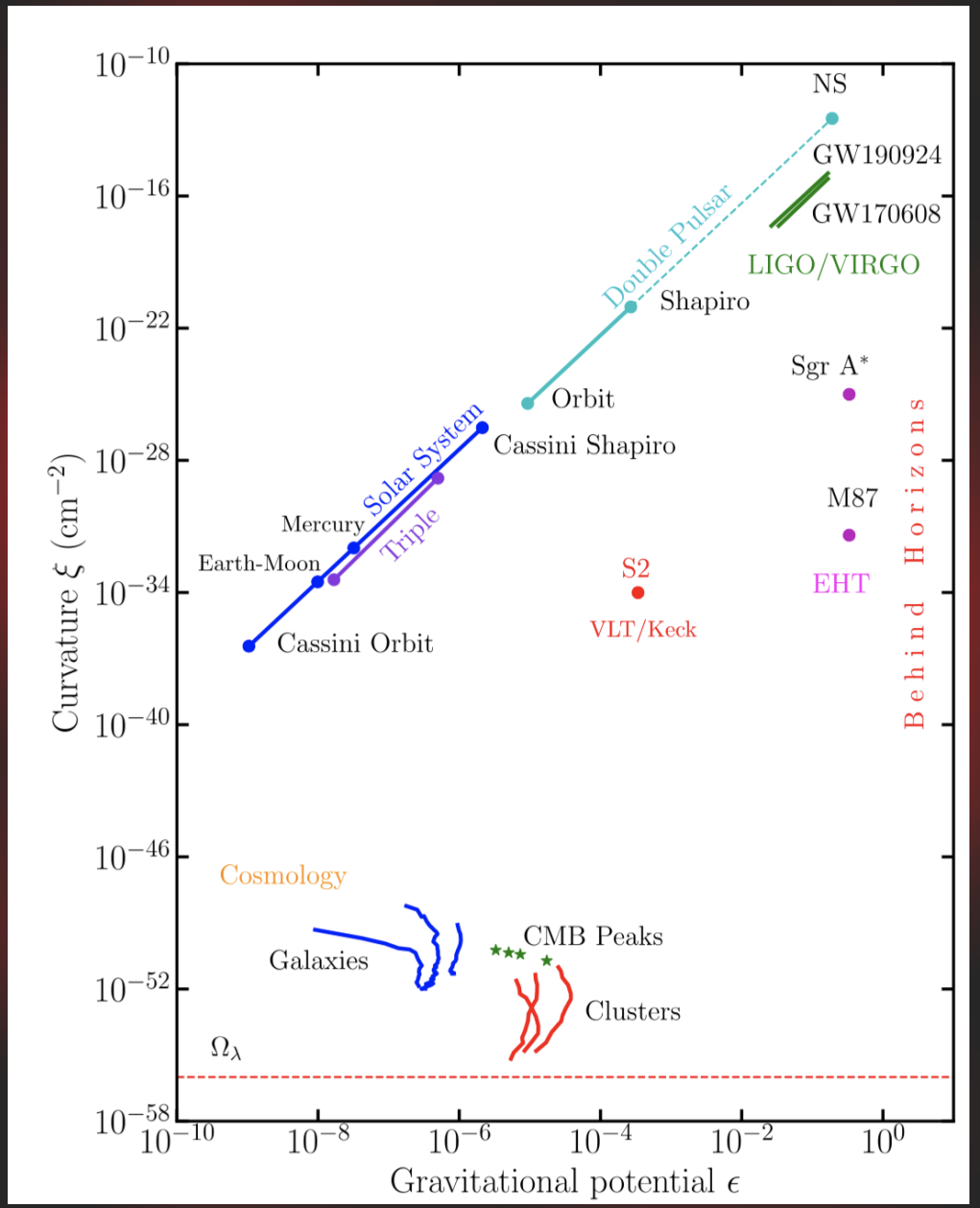

Primary EHT Results

- Black holes power active galactic nuclei
- EHT GR tests of BHs span 3 orders of magnitude
- Precision measurements of accretion and jet physics

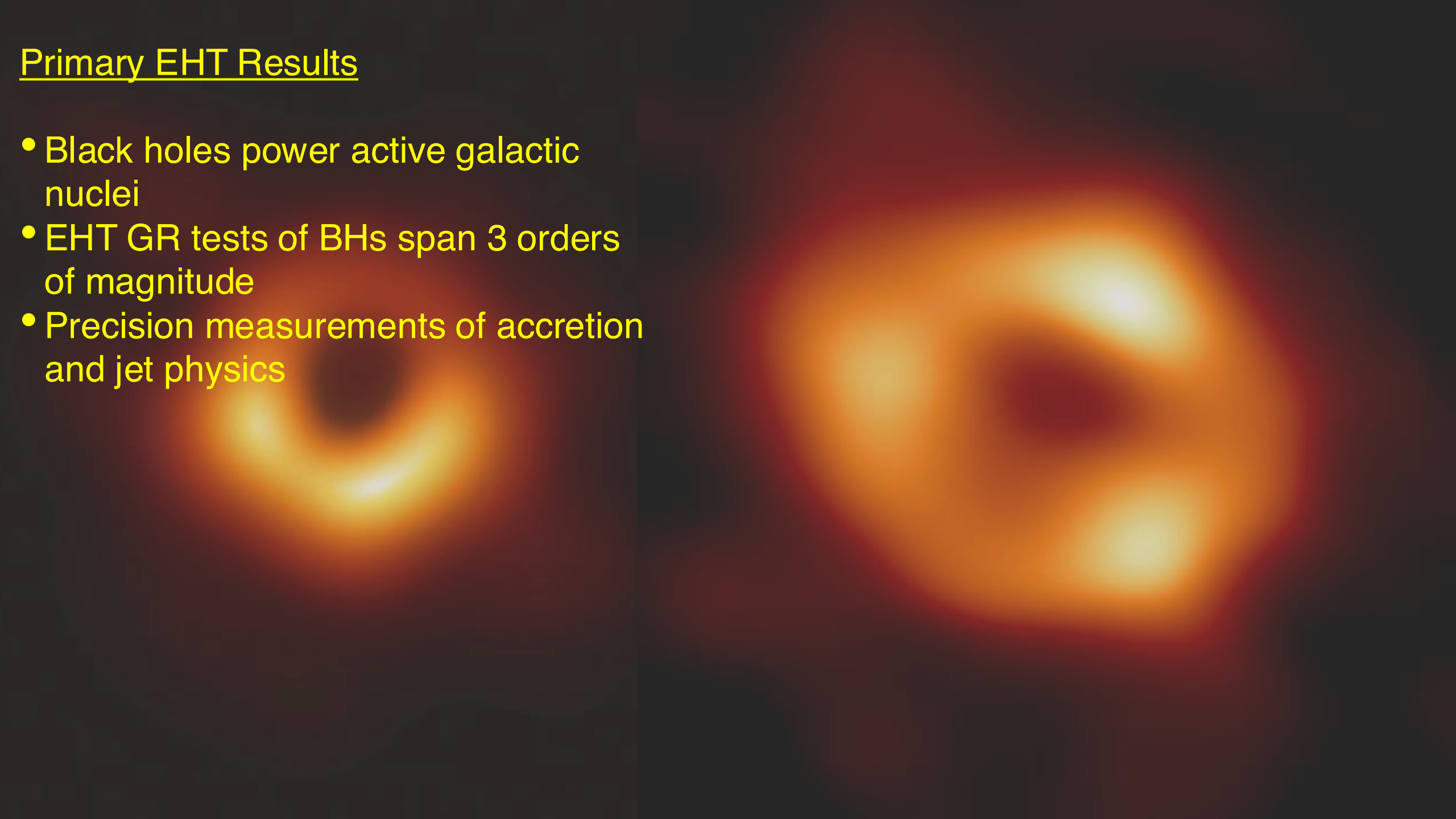

Primary EHT Results

- Black holes power active galactic nuclei
- EHT GR tests of BHs span 3 orders of magnitude
- Precision measurements of accretion and jet physics

Primary Questions for EHT Future

- What is the origin of relativistic jets in SMBHs?
- What causes flaring near SMBHs?
- Do SMBHs have strong magnetospheres that extract spin energy?
- What are the space-time properties of massive compact objects in galactic nuclei?

Q1: What is the origin of relativistic jets in SMBHs?

Goal 1: Establish the dynamical relationship between the SMBH and its relativistic jet in M87*

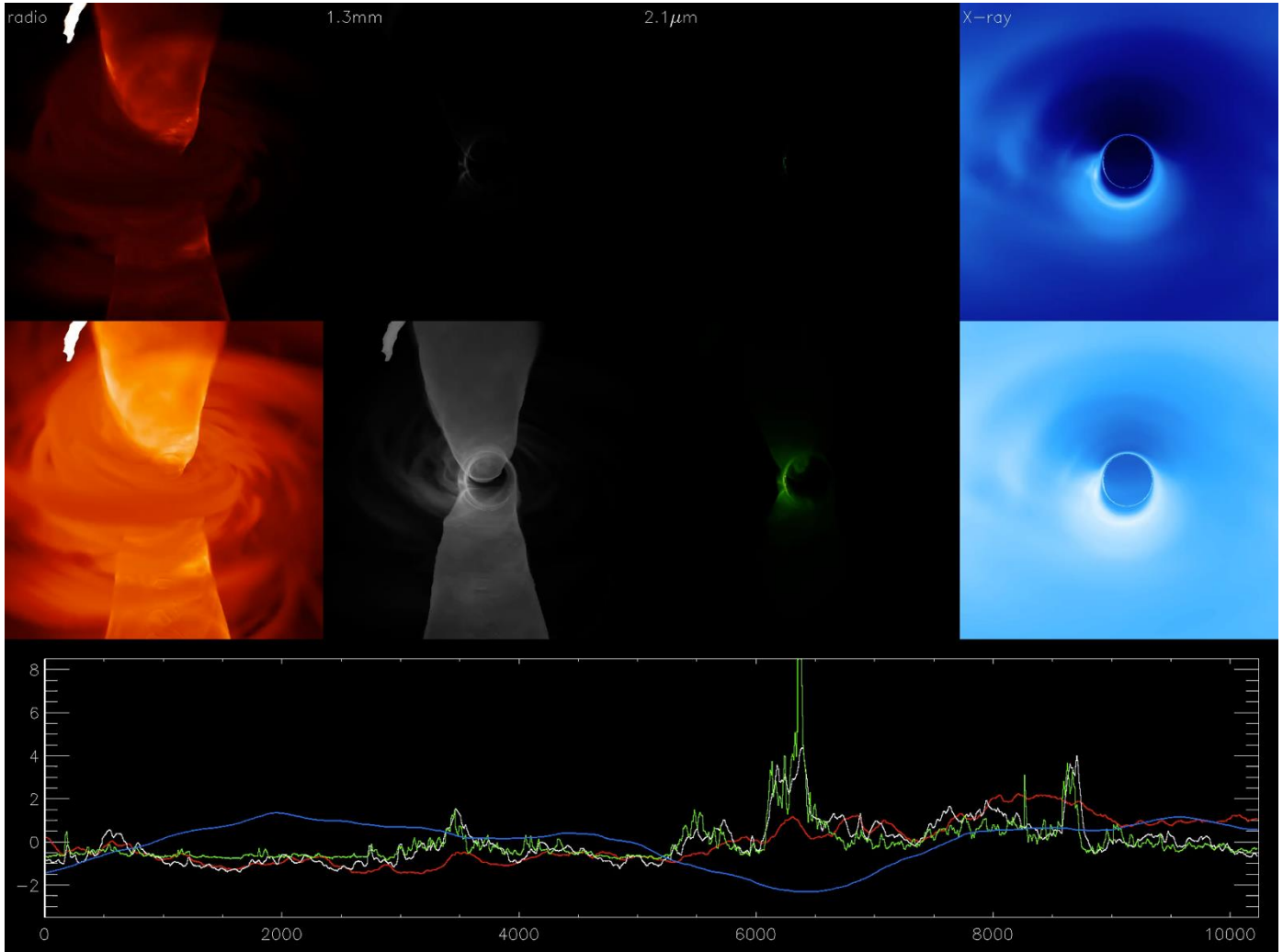

Characteristic variability is on monthly time scale

Q2: What causes flaring near SMBHs?

Goal 2: Measure the ring structure and dynamics of Sgr A*, especially during MWL flares

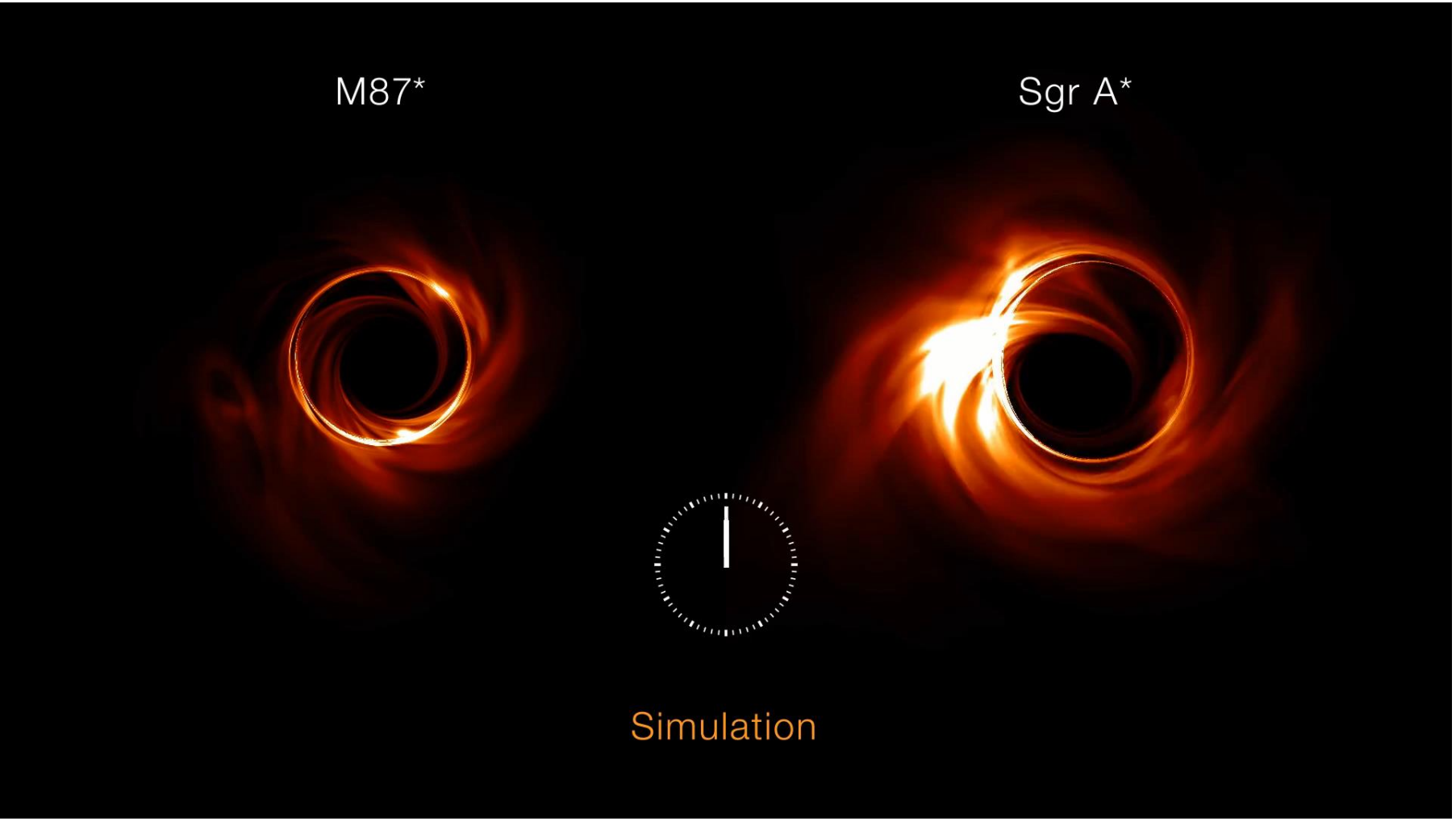

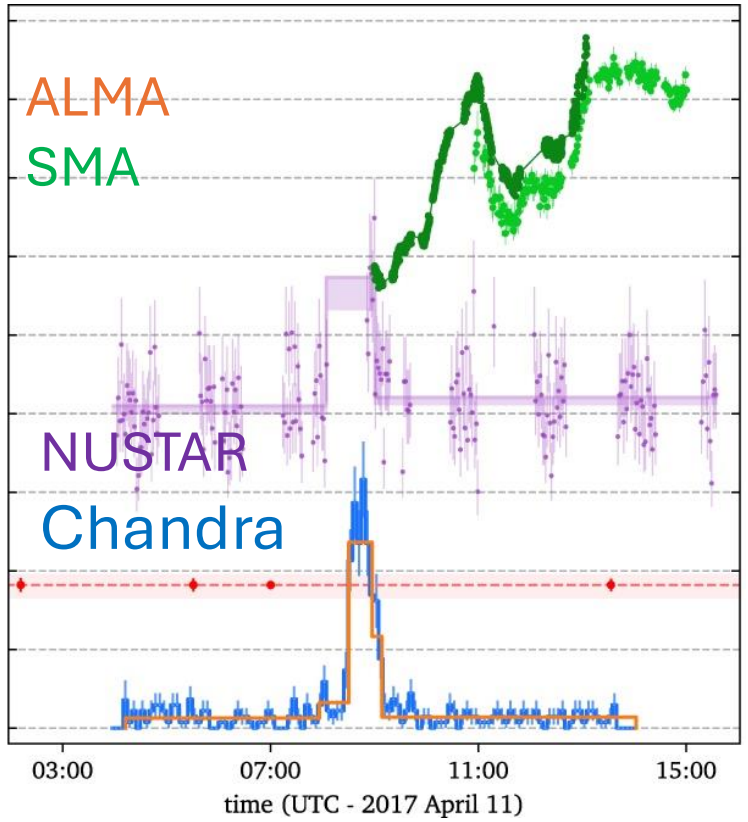

Q3: Do SMBHs have strong magnetospheres that extract spin energy?

Goal 3: Measure the near-horizon magnetic field structure and strength in M87* and Sgr A*

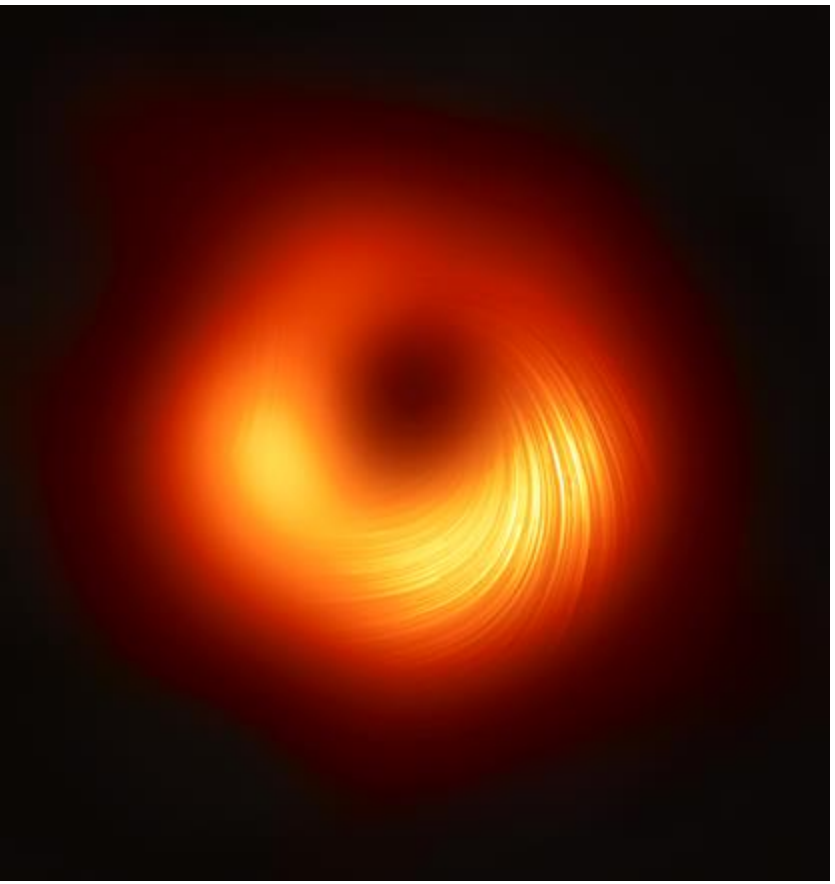

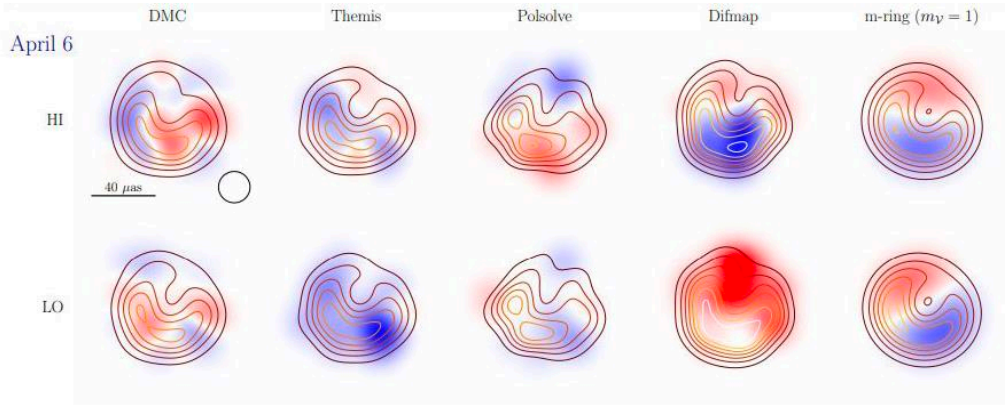

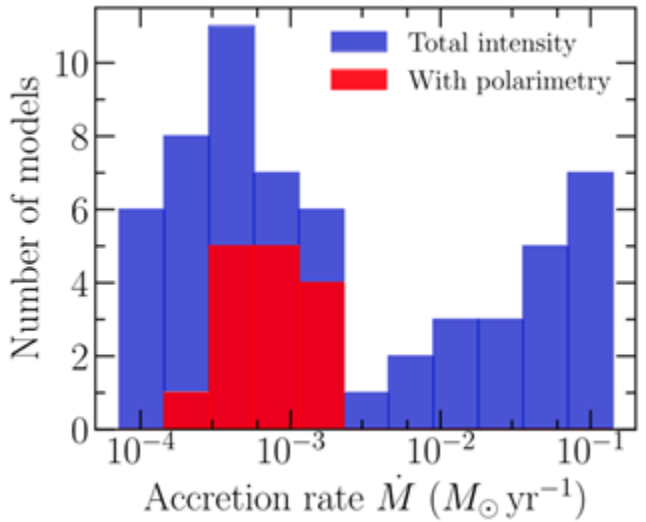

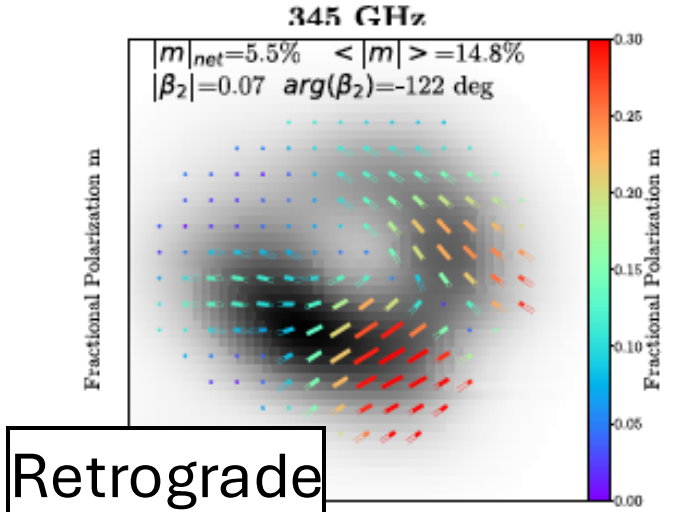

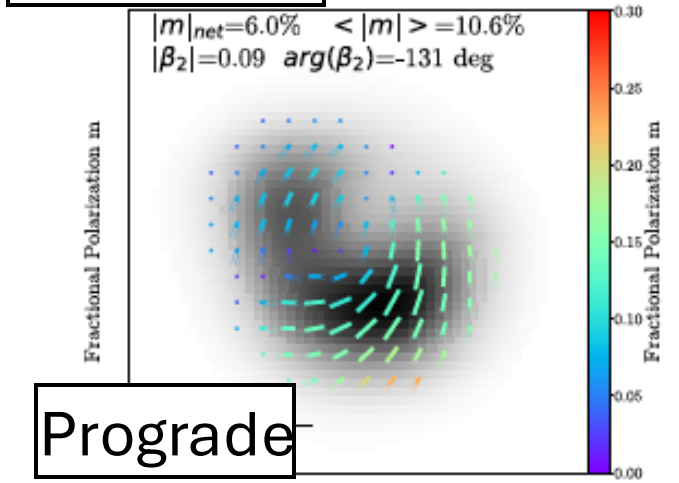

Q4: What are the space-time properties of the massive compact objects in galactic nuclei?

Goal 4: Estimate the spacetime properties for M87* and Sgr A* through properties of their emission rings and apparent shadows

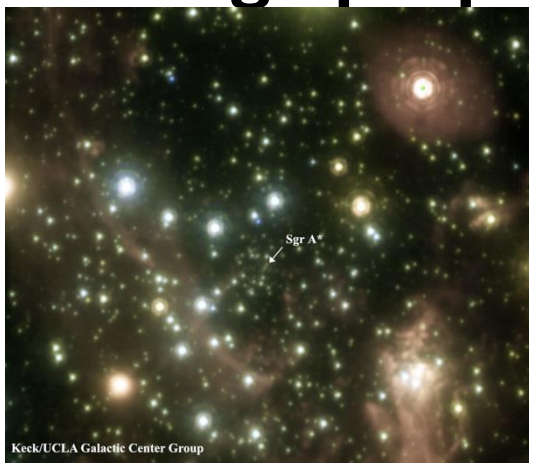

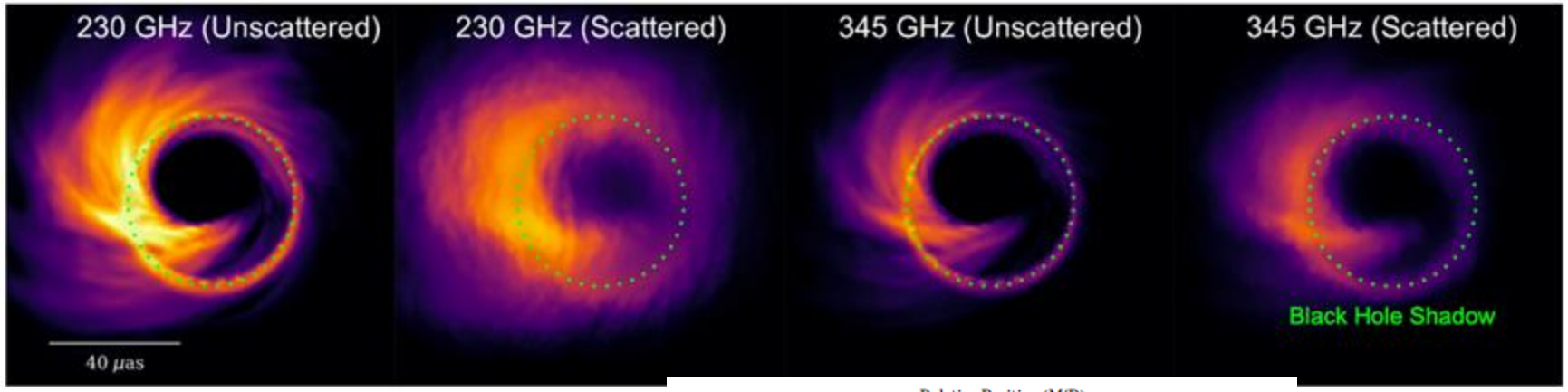

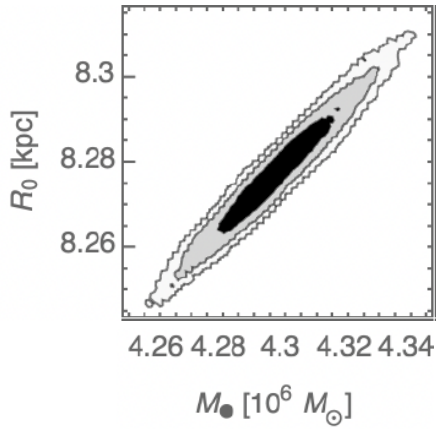

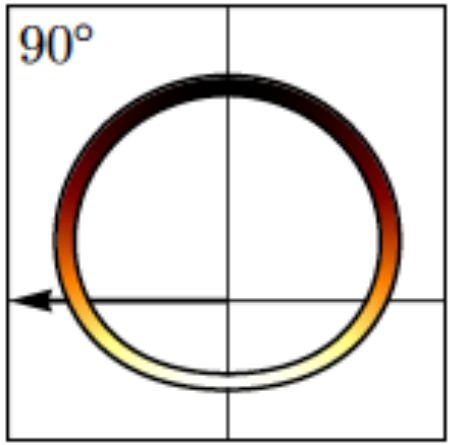

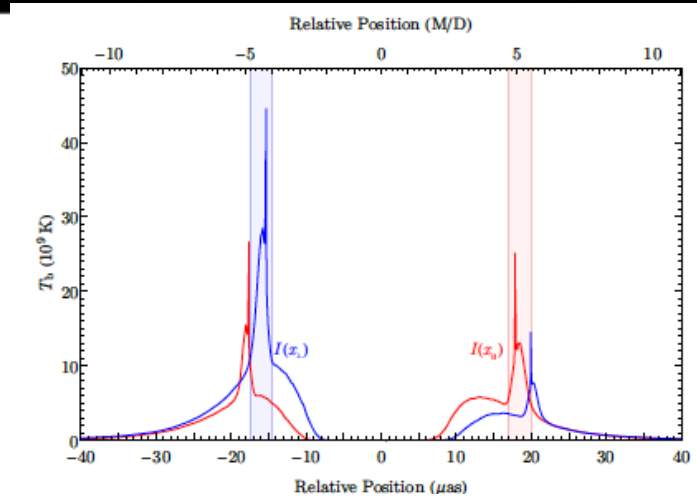

What’s Next for the Event Horizon Telescope?

Movie Campaign

- Jet/disk dynamic connection
- Stability of the ring image
- Deep image of the ring and jet
- Magnetic field structures

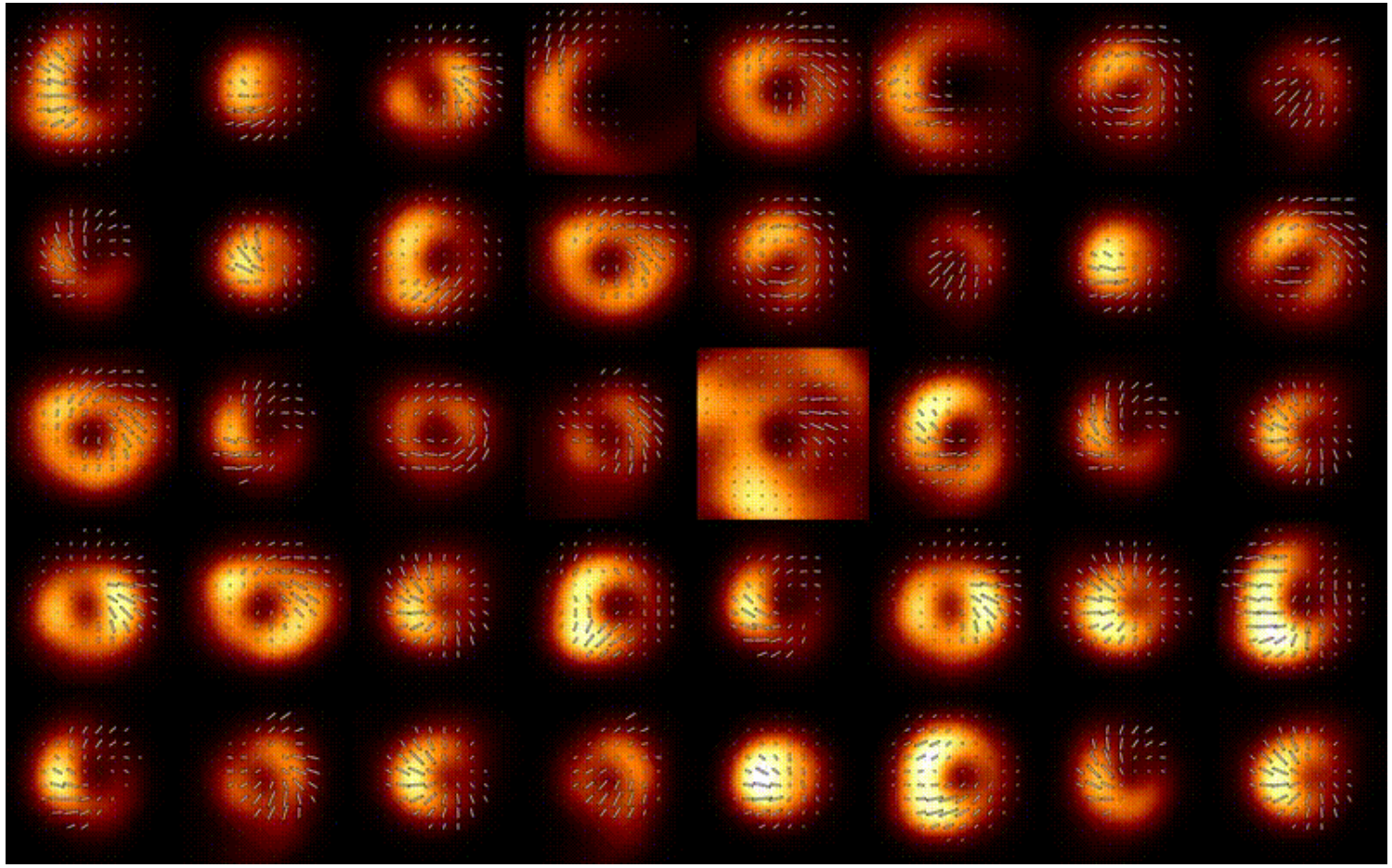

More observatories

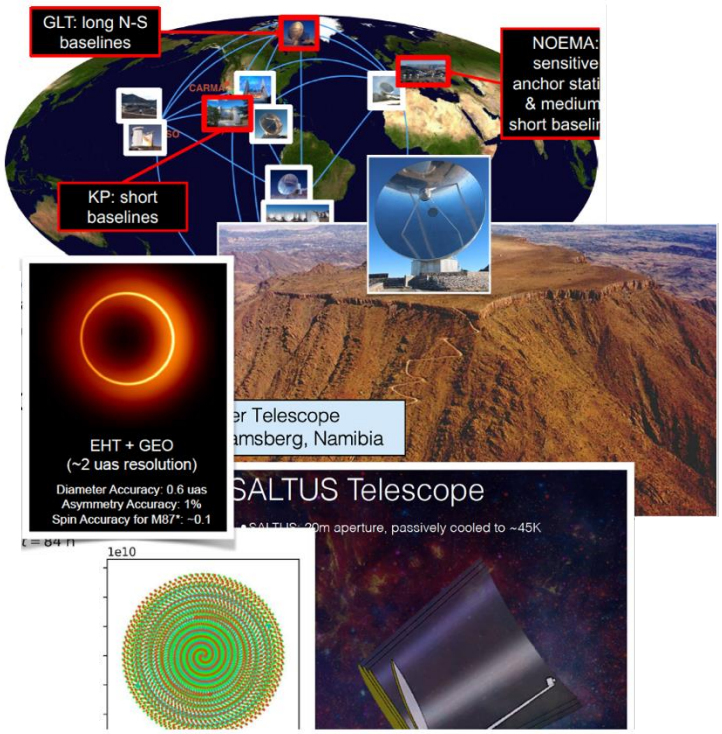

Wish list

- more antennas, better instantaneous coverage (… even in space!)
- Lower sensitivity limits, observe more AGN, spectral lines (masers, abs studies)

Multi-wavelength/messenger coverage to be further improved

The future is in space!

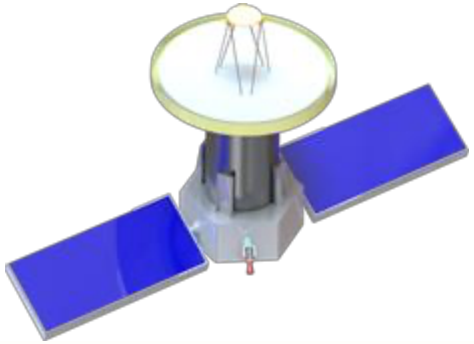

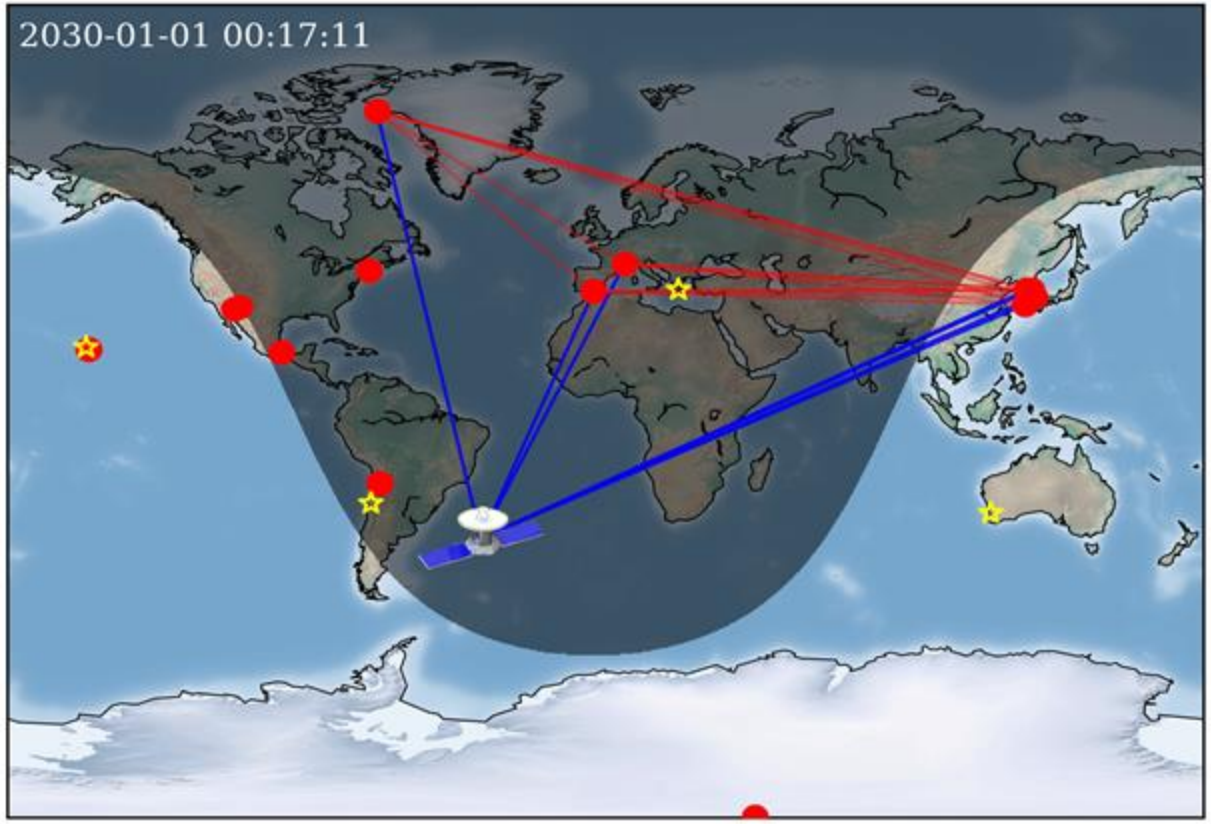

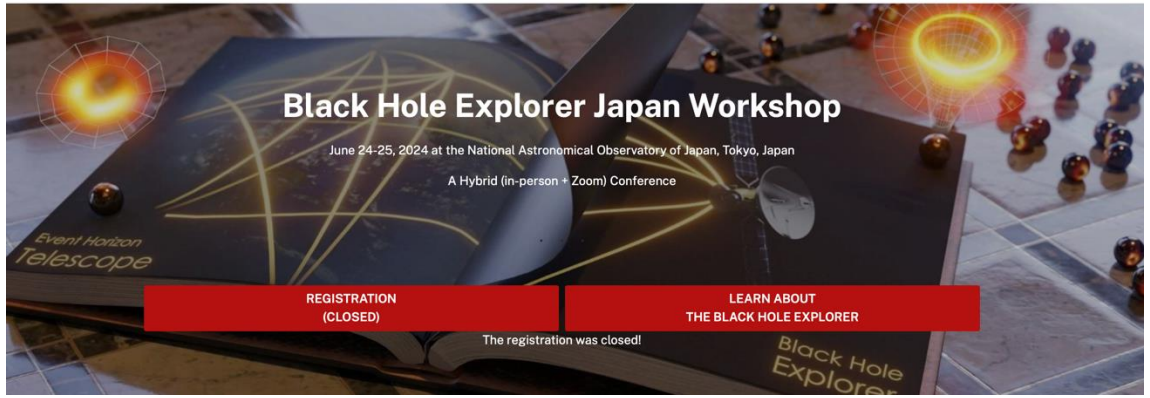

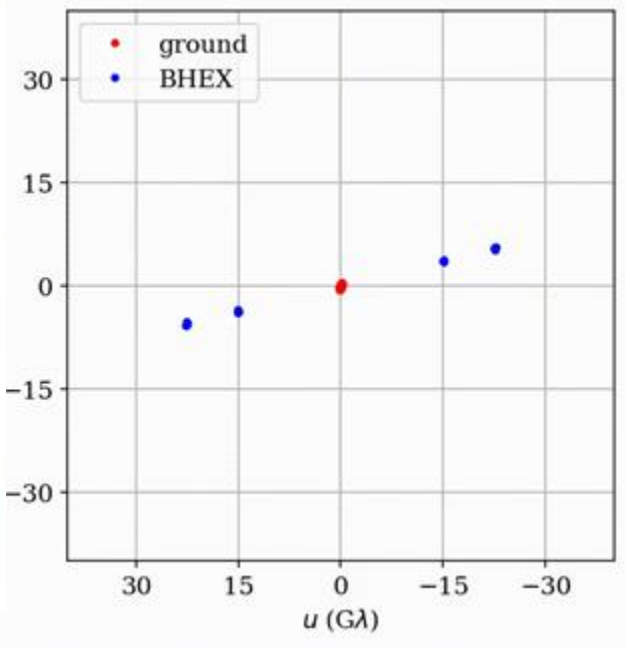

Ground VLBI observatories

BHEX

Ground optical terminals

PI Michael Johnson

The future is in space!

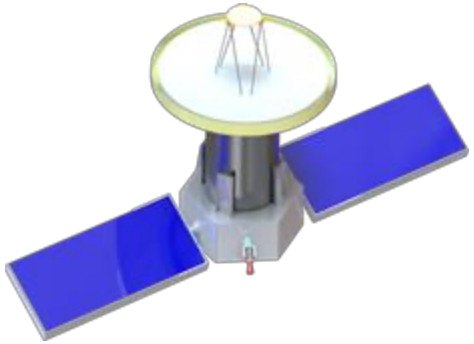

But see talks from Freek & Eric !

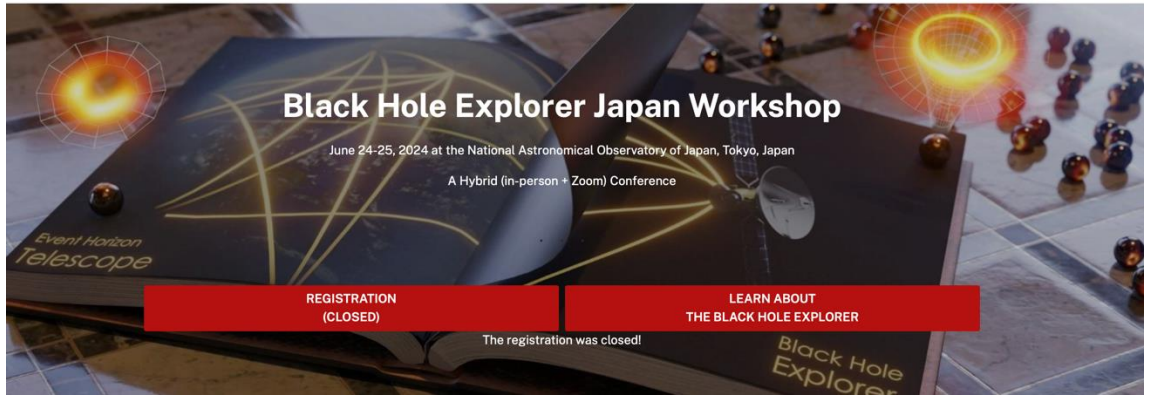

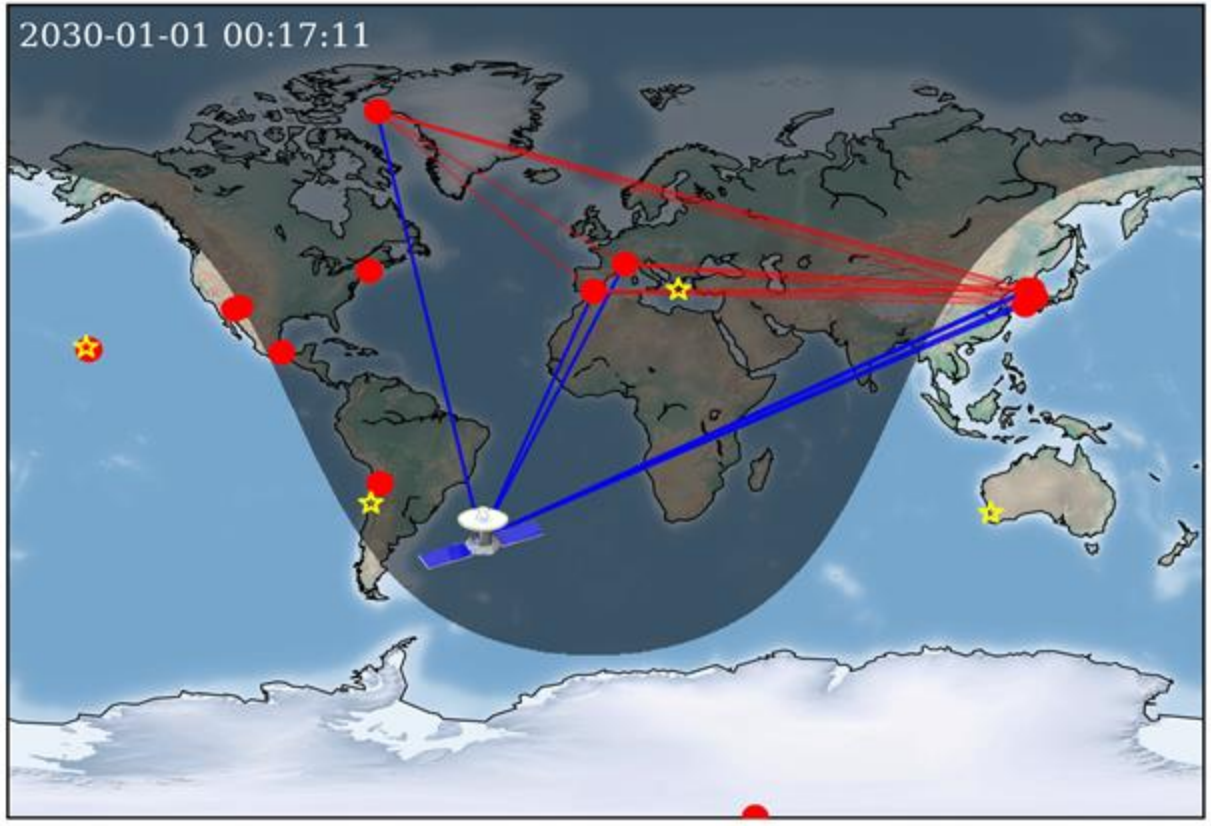

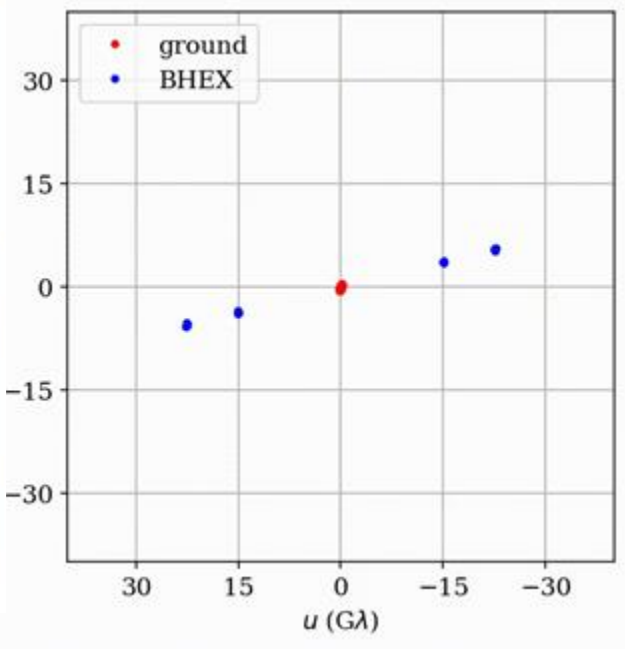

Ground VLBI observatories

BHEX

Ground optical terminals

PI Michael Johnson

Thanks for your attention